CHALMERS

Solid solution in the systems BiMO$_3$-ATiO$_3$ (M = Fe or Cr; A = Ba or Sr)

Synthesis, structure and magnetic properties

Master of Science Thesis in the Masters Degree Programme Materials and Nanotechnology

MARIA IRENE NIKUMAA

Department of Chemical and Biological Engineering

Division of Energy and Materials

CHALMERS UNIVERSITY OF TECHNOLOGY

Gothenburg, Sweden, 2010

Abstract

Compounds exhibiting more than one of the properties ferromagnetism, ferroelectricity and/or ferroelasticity, *i.e.* so called multiferroics, are promising materials for device applications. Co-existence of electric polarization and magnetization allows for a coupling between the properties, the so-called magnetoelectric effect, which mediate induction of magnetization through an applied electric field and vice versa. The research effort towards magnetoelectric materials has experienced a resurge during the last years. However, it is clear that in order to realize new technological applications it is necessary with further materials development. To understand the relationship between structure and properties, the principles of multiferroism and to predict new multiferroic materials, solid solutions of multiferroic materials have been studied.

For this thesis, polycrystalline samples of the binary solid solutions $x\mathrm{Bi}M\mathrm{O_3}$-$(1-x)A\mathrm{TiO_3}$ (M = Fe or Cr; A = Ba or Sr; x = 0, 0.2, 0.4, 0.5, 0.6, 0.8 and 1) were prepared by solid state sintering. Phase purity was analyzed by X-ray powder diffraction and it was determined that $\mathrm{BiFeO_3}$ formed binary solid solutions with both $\mathrm{BaTiO_3}$ and $\mathrm{SrTiO_3}$ for all measured x, while $\mathrm{BiCrO_3}$ did not form phase pure solid solutions with $\mathrm{BaTiO_3}$ and only partially with $\mathrm{SrTiO_3}$ (for $x \leq 0.5$). All successfully sintered samples showed cubic symmetry except for $0.8\mathrm{BiFeO_3} - 0.2\mathrm{SrTiO_3}$ which showed an onset of a transition towards a rhombohedral structure. Neutron time-of-flight data were collected from polycrystalline samples of $0.5\mathrm{BiFeO_3}$-$0.5\mathrm{BaTiO_3}$ and $0.5\mathrm{BiCrO_3}$-$0.5\mathrm{SrTiO_3}$ at room temperature and the subsequent structure model refinement revealed that the isotropic thermal vibration factors for the A-site was high, indicating disorder at that position and motivating further reverse Monte Carlo analysis of the total scattering. Magnetic measurements were carried out on the same samples, and $0.5\mathrm{BiCrO_3}$-$0.5\mathrm{SrTiO_3}$ showed an antiferromagnetic transition at 10 K, whilst the $0.5\mathrm{BiFeO_3}$-$0.5\mathrm{BaTiO_3}$ sample showed a ferromagnetic behavior.

Table of Contents

1 Introduction

Materials science is a significant research area in our present society, and our continuous technological development is depending on new and improved materials with suitable properties.[1] In the search for novel materials with the required qualities, it is important to understand the relationship between synthesis, atomic scale structure and bulk properties. A structural group of materials that has been the focus of extensive research is the perovskites. These are ceramic materials of the general formula ABX_3, where the *A*-site is occupied by a large cation and the *B*-site by a smaller cation. At the *X*-site position there is an anion, in many cases oxygen. The numerous permutations of cations and the many different distortions of the perovskite structure bring about materials with a range of properties. From this point of view, the perovskite structure enables ceramics with tailor-made qualities[2].

The ability for tailor-made properties makes the perovskite structure an interesting candidate for creating new and improved multifunctional oxide materials. Multiferroic materials are a group of multifunctional materials that simultaneously show one or more of the properties ferroelectricity, ferromagnetism or ferroelasticity[3]. Materials that are both ferroelectric and magnetic have the potential of exhibiting a coupling between these properties. This is the so-called magnetoelectric effect, and it brings about the possibility to change the electric polarization by an external magnetic field and vice versa[4-8]. The aspect of controlling magnetism by electric field renders magnetoelectric multiferroics interesting for applications such as sensors, memories, modern optics and spintronic devices[9-14].

Unfortunately, magnetoelectric multiferroics are very rare. This is due to the conflicting nature of the microscopic origins of ferroelectricity and magnetism[15]. Conventional structure-property mechanisms contradict the co-existence of these two properties. Nevertheless, materials exhibiting both ferroelectricity and ferromagnetism exist and therefore alternative explanations of the physical phenomena have been formulated. In bismuth-containing perovskites such as $BiFeO_3$, $BiMnO_3$ and $BiCrO_3$, ordering of the unpaired d-electrons of the transition metal can cause a macroscopic magnetization. Simultaneously, the stereochemically active $6s^2$ lone-pair of the bismuth cation can drive an off-centering of the cation that results in ferroelectricity.

A drawback is that these perovskites have proven difficult to synthesize. Another disadvantage is that even though $BiFeO_3$ has the rare property of being multiferroic at room temperature, very strong fields is needed to influence the magnetization and electric polarization. Further materials research is needed in order to find more easily synthesized materials with strong enough magnetoelectric coupling at room temperature. Enhancement of the "ferroic" properties and the magnetoelectric effect in multiferroic materials may be achieved by forming solid solutions. Motivated by previous work on $BiMnO_3$ in solution with $BaTiO_3$ and $SrTiO_3$[16], the subject of this thesis is the synthesis, structure and magnetic properties of the binary solid solutions $x\mathrm{Bi}M\mathrm{O}_3$-$(1-x)A\mathrm{TiO}_3$ (*M* = Fe or Cr; *A* = Ba or Sr; *x* = 0, 0.2, 0.4, 0.5, 0.6, 0.8 and 1).

2 Background

2.1 The Perovskite structure

Calcium titanate, $CaTiO_3$, is a natural mineral that was first described by Gustav Rose in 1839. He named it perovskite, in honor of the Russian mineralogist Count Lev Alexejevitj Perovskii. Perovskite is also the name for a general structure. The ideal perovskite is a cubic structure belonging to space group $Pm\bar{3}m$, although naturally occurring $CaTiO_3$ adopts an orthorhombic structure. A compound better describing the ideal perovskite structure is $SrTiO_3$.[2]

The general formula for the ideal perovskite is ABX_3, where the *A* and *B* species are cations. At the *X*-site position is an anion similar in size to the *A*-cation, while the *B*-cation is typically smaller. An array of corner sharing anion BX_6 octahedrons builds the structure. The *B*-cation is positioned in the centre of the octahedrons surrounded by six *X*-anions at the corners and the *A*-cation in the interstices. Consequently, the *A*-site cation is positioned in the centre of twelve *X*-anions in cuboctahedral coordination (***Figure 2-1***). Another way of viewing the ideal perovskite structure is as close-packed layers of *A* and *X* ions with 25% of the octahedral holes occupied by the *B* ions.[17] The ideal perovskite structure can be depicted in different ways, commonly with the *B*-site at the origin, *A*-site at the centre of the cell and the *X*-site at the middle of the edges. This is called the *B*-cell setting. In the *A*-cell setting, the origin is located at the *A*-site, placing the *B*-site at the centre of the cell and the *X*-site at the centre of the cubes faces.

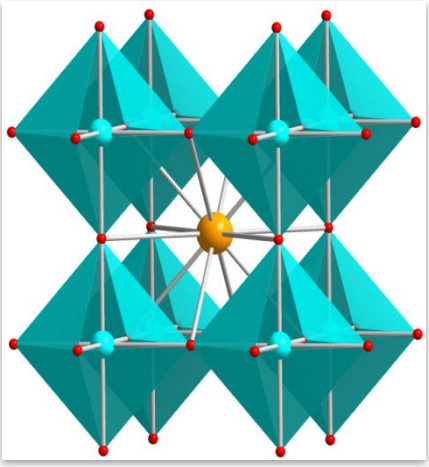

Figure 2-1: *The ideal perovskite structure. At the center of the blue octahedra are the B-sites (blue spheres), surrounded by six X-sites (red spheres). In the middle is the cuboctahedral A-site (yellow sphere).*

Perovskites are considered to be ionic compounds, and the ions can be regarded as spheres with ionic radii *R*. In 1926 Goldschmidt[18] observed that at a certain pressure and temperature, the

prediction whether an assembly of ions will form an ideal perovskite structure can be guided by a relative ratio of the ionic radii called the *tolerance factor, t:*

$$t = \frac{R_X + R_A}{\sqrt{2}(R_X + R_B)}$$

When the tolerance factor is close to 1, the ideal cubic symmetry is expected. However, distorted perovskite structures can exist in the approximate range 0.78< *t* <1.05. It should be noted that the tolerance factor is only a guideline; it does not solely determine the structure. The formation of a perovskite structure is governed by a range of additional factors including the accuracy of approximating the perovskite as an ionic compound, metal-metal interaction, Jahn-Teller distortions and lone pair effects[19-21]. Many types of different distortions from the ideal structure (such as tilting of the BX_6 octahedra and off- centre displacement of the *A*-cation) can occur in the perovskite crystals. In combination with the flexibility of choice of ions and substitution of ions, this enables various perovskites with a multitude of physical properties. Examples of technologically interesting properties displayed by perovskite materials are: superconductivity, colossal magnetoresistance, ionic conduction and a range of dielectric and magnetic properties.[22]

2.2 Multiferroic materials and the magnetoelectric effect

Multiferroic oxide materials are attractive for device applications due to the coexistence of more than one technologically interesting property, which is a desirable quality *e.g.* in the view of device miniaturization and energy efficiency. The multiferroic materials simultaneously exhibit more than one of the "ferroic" orderings ferroelectricity, ferromagnetism or ferroelasticity, as defined by Schmid[3] in 1994. However, the term has later broadened to also include ferrotoroidic and antiferroic order.[9]

Multiferroic materials that are both ferroelectric and ferromagnetic in the same phase, magnetoelectric multiferroics, have the potential for a variety of applications. Magnetoelectric materials have the possibility to show a coupling between the properties, the so-called magnetoelectric effect. The magnetoelectric effect brings about control of the materials magnetization through an electric field and control of the electric polarization through an applied magnetic field. These new functionalities allows for a range of novel devices. Examples of suggested applications include memory devices, transducers, modern optics and spintronics[12-15]. The research on the magnetoelectric effect is focused on the linear response of polarization and magnetization. Higher orders magnetoelectric effect also exist, however, these effects are much smaller than the linear counterpart. The expression "the magnetoelectric effect" without any prefixes generally refers to the linear manifestation of the phenomena.

The magnetoelectric effect was predicted as early as 1894 by Pièrre Curie and first observed in 1959[23]. In the 1960s and 1970s a number of studies of magnetoelectric materials were performed

(see Loidl[13] 2008 and Fiebig[10] 2005 and references therein). The possibility for technical applications was early recognized. However, after this decade of research, the interest in the area declined, probably due to the very few materials found, low temperatures needed and limited understanding of the microscopic sources for the magnetoelectric effect. The activities stayed low for the following two decades, until it was revived in the late 1990s, made possible by the developments in sample characterization, thin film production, composites and nanostructures. New instrumentation to analyze the physical properties of the materials, modeling and theoretical tools have led to the discovery of the "giant magnetoelectric effect", were the electric or magnetic field not only induce magnetization or polarization, but triggers magnetic or electric phase transitions[24]. All of these developments have contributed to the renaissance of multiferroic materials.[25] For future device applications, thin films and nanostructures will most likely be of interest.[26,27] Even so, it is still important to study bulk single-phase multiferroic materials, to increase the understanding of the origin of ferroelectricity, magnetism and the coupling between these properties.

The technical expectations of magnetoelectric multiferroics have been high, but the experimental and theoretical research has revealed many problems in the area. Few magnetic ferroelectric materials have been discovered and many times proved to be difficult to synthesize. The coupling between the properties has shown to be weak, high fields have been needed to induce polarization and in most cases the magnetoelectric effect only manifest at low temperatures. Also, the question of the underlying phenomena for the coexistence of ferroelectricity and magnetism needs further theoretical work, much of it which is out of scope for this text.

As mentioned above, materials that are both electrically polarizable and magnetic are very rare. There are many technologically important perovskites with ferroelectric properties; *e.g.* $BaTiO_3$ and (Pb, Zr)TiO_3. There are also a number of magnetic perovskite structured oxides; *e.g.* $CaMnO_3$ and $YMnO_3$, so it seems that both ferroelectricity and (anti-) ferromagnetism are properties frequently found in perovskites. However, the two properties does not co-exist in any commonly used perovskite and only in a very few known ceramics of scientific interest. The scarcity of magnetoelectric materials is due to the microscopic origins of ferroelectricity and magnetism and symmetry considerations. Conventional explanations of the two properties contradict their co-existence in one phase. In a ferroelectric perovskite, the electric polarization is explained as caused by an off-centering of the small transition metal ion within the oxygen octahedra. The ferroelectric phase is then stabilized by bonds created when charges transfers from the filled oxygen orbital to the empty *d* states (or *f* states) of the transition metal ion. In contrast, magnetism is caused by ordering of the magnetic moment of unpaired electrons and hence need transition metal ions with partly filled *d*- or *f*-shells. The *d*-electron (or *f*- electron) charge density of the *B*-site cation in a magnetic perovskite is spherically symmetrical distributed, and therefore resist displacement, which contradicts the existence ferroelectricity. Hence, the requirements for ferroelectricity and (anti-) ferromagnetism are mutually exclusive.[28,29]

In magnetoelectric multiferroics, at least one of the properties has to come about by an alternative mechanism. There are a couple of ways described, such as: charge ordered multiferroics, geometrically frustrated multiferroics and magnetically driven ferroelectricity[30-32]. The perovskite oxides subject to this thesis enable multiferroism through another mechanism involving the stereochemically active lone-pair electrons of the large Bi^{3+}-cation occupying the *A*-site. The small *B*-site cation is a transition metal ion, responsible for the ferromagnetic properties and so has a partly-filled *d*-shell. The *d*-electron charge density resists displacement and no electric polarization is possible. Ferroelectricity can then not be caused by the transition metal ion. For the material to be magnetoelectric, the off-centering needed for electric polarization must come about by an alternative mechanism. The $6s^2$ lone-pair electrons of the *A*-site Bi^{3+}-cation can stabilize an off-center distortion of the Bi^{3+}-cation within the oxygen cuboctahedra, which creates a structural distortion and enables electric polarization[33].

2.3 The parent oxides and the solid solutions

The subject of this thesis is binary solid solutions of the perovskites $BiFeO_3$, $BiCrO_3$ with $BaTiO_3$, $SrTiO_3$ (a total of four solid solution series). This subsection concerns the four "end" members of the solution series, their structure, properties and most important applications.

Bismuth ferrite, $BiFeO_3$, has gained scientific interest due to its rare quality of being both ferroelectric and antiferromagnetic at room temperature. It was long debated whether bismuth ferrite was ferroelectric or not until Tabares-Munoz *et. al.* settled the question when they observed ferroelectric/ferroelastic properties using polarized light microscopy[34]. At ambient conditions, $BiFeO_3$ has a rombohedrally distorted perovskite structure assigned to the space group *R*3*c*. The ferroelectric transition temperature, $T_C \approx 830$ °C, and the antiferromagnetic transition temperature $T_N \approx 370$ °C.[35] The electric polarization prefers to align along the [111] direction, [36] and it is usually weak, possibly due to high leakage currents[28]. It is antiferromagnetic, but the spins are not collinearly ordered, but rather ordered spirally, in a cycloid structure of wavelength 62 nm[37]. The winding of the magnetic moments makes the linear magnetoelectric effect to average to zero in the bulk material, unless the spiral is coerced to unwind by a strong magnetic field. On the other hand, in epitaxial thin films, the winding is constrained to a slight canting of the spins. [9]

Another bismuth-containing ceramics that has been suggested as a candidate for multiferroism is $BiCrO_3$[38]. It has antiferromagnetic order with $T_N \approx -164$ °C, and the antiferromagnetic phase has a monoclinic structure and belongs to the space group *C*2*/c*. The material has to be synthesized at high pressures (about 6 GPa) and high temperatures (in the range of 1400 °C) [39]. Multiferroism in both bismuth ferrite and bismuth chromate comes about by the mechanism described in the previous subsection. That is, the small transition metal ion (Cr^{3+} or Fe^{3+}) has unpaired electrons that can align their spins in an antiferro-, ferri- or ferromagnetic way. The stereochemically active $6s^2$ lone-pair electrons of the Bi^{3+}-cation distort the ions position and enables polarization.

A ferroelectric perovskite of technological importance is barium titanate, $BaTiO_3$. It has a tetragonal structure (space group *P4mm*) with a spontaneous polarization that can be reversed by an external electric field, and the polarization will show a hysteresis loop upon reversal. Off-centering of the small transition metal cation is favored by the donation of electron density from the filled oxygen 2*p* states into the empty *d* states of the displaced titanium ion. Above the Curie temperature, $T_C \approx 120$ °C,[2] the short range repulsions between adjacent electron clouds will predominate. As one suggested model explains, these forces will push the Ti^{4+} cation back to the centre of the oxygen octahedra and a phase transition from the tetragonal ferroelectric phase to a cubic, symmetric, un-polarizable and hence non-ferroelectric phase. At temperatures lower than room temperature, the structure will undergo transition from tetragonal to orthorhombic to rhombohedral. In all phases but the cubic phase, hybridization between Ti 3*d* and O 2*p* states stabilizes an electric polarization. In the tetragonal phase the polarization is along the [001] axis and the Ti^{4+}-ion is surrounded by four equally distant (2.00 Å) oxygen ions in the equatorial plane and the two oxygen above and below that plane has one a shorter bond length (1.857 Å) and one has a longer bond length (2.177 Å). Hence, $BaTiO_3$ is ferroelectric in all phases except the high-temperature cubic one. [15,40,41]

$SrTiO_3$ adopts the ideal simple cubic perovskite structure and has the space group $Pm\bar{3}m$. It is widely used for technological applications, *e.g.* as a substrate for epitaxial growth of high-temperature superconductors and in optics. At room temperature strontium titanate is paraelectric and at very low temperature it becomes superconducting (T_C = -272.8 °C)[42].

Why study solid solutions? It is the multiferroic properties of $BiFeO_3$ and $BiCrO_3$ that is desired, why dilute them with compounds with only one or none ferroic order? One reason is that $BiFeO_3$ and $BiCrO_3$ unfortunately are quite difficult to synthesize. Diffraction patterns commonly show formation of impurity phases. It is also extremely difficult to grow even minuscule single crystals, commonly polycrystalline samples are prepared. Solid solution with $BaTiO_3$ or $SrTiO_3$ could result in a multiferroic material obtained by a simpler synthesis. Although pure $BiCrO_3$ has to be synthesized at high pressures, solid solutions of $BiCrO_3$-$SrTiO_3$ up to 70 mol% have been reported to form at ambient pressure and temperatures below 1300 °C[43]. Another reason to form solid solutions is to find materials with stronger ferroic ordering, because the magnetoelectric effect cannot be stronger than the inherent strength of the ferroelectric and (anti-)ferromagnetic properties. $BiFeO_3$ has a cycloid ordering of the magnetic moment, which causes the linear magnetoelectric effect to average out to zero. Chemical substitution may result in a material with another magnetic structure. Other materials disadvantages might also be better understood when studying solid solutions, the insights and theories may aid prediction of novel materials with the wanted properties

The ferroelectric properties of $BiFeO_3$ have been extensively studied. Bismuth ferrite exhibits a surprisingly low polarization in single crystals, bulk and thin films, and it has been explained by high leakage currents. The leakage current is due to the low resistivity of bismuth ferrite. Small amounts

of bismuth-rich secondary phases such as $Bi_{40}Fe_2O6_3$ and $Bi_{36}Fe_2O_{57}$ are commonly found in polycrystalline samples of $BiFeO_3$ and the segregation of these secondary phases at the grain boundaries could play a role in lowering the resistivity of the material. Unfortunately, the low resistivity and the resulting low polarization inhibit the ferroelectric hysteresis loop, which limits the application of the compound. Reduced formation of impurities and enhanced ferroelectric properties has been reported for $BiFeO_3$ in solid solution with other ABO_3 perovskites, including $BaTiO_3$. Lower amount of impurities results in a more distinctive hysteresis loop. The addition of $BaTiO_3$ has also shown to effect the formation of the grain size, which in turn influences the conductivity[44-46]. New synthesis methods, such as liquid-phase rapid sintering, have also shown to increase the magnitude of the polarization in bismuth ferrite[28].

2.4 Motivation and aim of the project

The project involves the synthesis and structure of the four solid solution series $x$$BiFeO_3$-(1-$x$)$BaTiO_3$, $x$$BiFeO_3$-(1-$x$)$SrTiO_3$, $x$$BiCrO_3$-(1-$x$)$BaTiO_3$ and $x$$BiCrO_3$-(1-$x$)$SrTiO_3$. The choice of solid solutions is motivated by previous work on binary solid solutions of the multiferroic perovskite $BiMnO_3$ with $BaTiO_3$ and $SrTiO_3$[16]. As mentioned above, $BiFeO_3$ and $BiCrO_3$ are candidates for magnetoelectric multiferroic materials. To improve the ferroelectric characteristics, solid solutions with other perovskites with better ferroelectric and dielectric properties have been formed. These other perovskites include $BaTiO_3$[47,48], $SrTiO_3$[43], $PbTiO_3$[49] and $PbZrO_3$[50]. Since there is a demand on lowering the amount of lead used in laboratories and industries, Pb-containing compounds were not selected as suitable candidates.

This thesis is a pre-study of solid solubility in these systems, intended to lead to an investigation of both long- and short-range atomic scale structure by reverse Monte Carlo (RMC) analysis of total neutron scattering data. Insights from this project and subsequent RMC analysis are intended to improve the understanding of the relationship between structure and properties, in particularly the role of displacement of the large A-site cation in perovskites. The long-term aim is to improve the models of coexistence and coupling of ferroelectric and ferromagnetic properties, and thereby aid the prediction of new magnetoelectric multiferroic materials with potential for novel high-technology device applications.

3 Experimental methods and theory

3.1 Solid state sintering

A basic way to prepare solid materials is the high temperature ceramic method, also called *solid state sintering route*. The synthesis is straight-forward; stochiometric amounts of solid reactants are grinded and heated in a furnace. The reaction occurs at the grain surfaces, and to maximize the grain contact, the powders can be compacted to pellets in a hydraulic press. For completion of the reaction, the process may be repeated several times, with intermediate grinding and pressing and at increasing firing temperatures. The start materials are commonly oxides and carbonates of the wanted species and the mixture is placed in a crucible made of a non-reactive material that can withstand high temperatures, *e.g.* alumina or platinum. For the first heating, the temperature should be less than the lowest melting temperature of the constituent reactants. In this way, the specie with the low melting point will be incorporated with the other reactants before the temperature is raised. In the subsequent heating cycles, the temperature needs to be raised until the reaction has completed. The phase purity is determined with powder X-ray diffraction between the heating steps.

The reaction generally occurs in the solid state, at the interface of the solid grains. Atoms in the start materials have to leave their position and diffuse to a different lattice site. When the outer layer of a grain has reacted, the atoms have to diffuse from the bulk of the grain to the surface for the reaction to continue. This diffusion is often the limiting step in the reaction. To ensure large reaction area and minimize the need of diffusion through distances within the grains, it is important to grind thoroughly. The intermediate grinding between heating is thus important for enabling fresh reactant surfaces and to increase homogeneity of the product. The grinding can be done by hand with a mortar and pestle. The material of the mortar should be hard and non reactive. Commonly occurring materials for mortars are alumina and agate stone. The grinding can also be done in a milling machine, *e.g.* in a rotary ball mill such as the *Fritsch Pulverisette 7* (***Figure 3-1***).

Figure 3-1*: Fritsch Pulverisette 7 rotary ball mill.*

The simplicity of the solid state sintering route is its main advantage, and the method is widely used in both industries and laboratories. On the other hand, the method has several drawbacks. The cause for most of the disadvantages is the large amount of energy needed for an atom to overcome the lattice energy and diffuse to a different position. To speed up the diffusion, high temperatures is needed, typically between 500 to 2000 °C and this requires a large energy input which is costly. High temperatures can cause problems such as evaporation of reactants and decomposition of the product. It can also be difficult to obtain phase purity, since the reaction occurs at the surfaces and the diffusion of unreacted atoms through the solid material is low. Formation of impurity phases can be troublesome since it is usually not possible to purify solid materials once they have formed.

3.2 Characterization methods

This subsection features a description of the methods and the theory behind atomic scale structure characterization and magnetization.

3.2.1 Diffraction methods

Diffraction is a powerful method of studying atomic structure[22,51-55]. Light in the visible range has too long wavelength (not energetic enough) to interact with the atom planes. Particles with shorter wavelength, in the order of twice the interatomic distances or less, such as electrons, X-ray photons or neutrons, can be used in diffraction experiments. Surfaces and thin films are probed with electrons (not used in this project), while bulk materials are analyzed with X-rays and neutrons. The subsections below discuss the relationship between structure and scattering, and the two methods X-ray powder diffraction and neutron powder diffraction.

3.2.1.1 Structure and scattering theory

Atoms don't ever sit still. In a gas or liquid they move throughout the available volume, and their movement can be described by probability distributions of instantaneous distances between atoms. Solid materials are composed by atoms that behave in a different way, instead of moving about long distances, they are defined to move back and forth about an equilibrium position. In crystalline solids, the time-averaged positions of the atoms are ordered regularly over large distances. This structure, the atoms occupying the sites and their mean movement about their positions, is unique to each crystalline compound and determines the properties of the material.

The periodicity of the atoms is described by an array of repetitive unit cells, attached to a metaphysical three-dimensional lattice. In real space, the crystal structure is described by a set of three basis vectors $\boldsymbol{a}$, $\boldsymbol{b}$ and $\boldsymbol{c}$ that define the size and shape of the unit cell. By elementary vector analysis, the cell volume is $V = |\boldsymbol{a} \cdot \boldsymbol{b} \times \boldsymbol{c}|$. Planes and directions in crystals are denoted by *h, k, l,*

where (*hkl*) denotes planes and [*hkl*] denotes a direction perpendicular to that plane. There are four types of lattice centerings and seven possible crystal systems, combined they produce the 14 permissible Bravais lattices. Crystal symmetry can be described by 32 point groups, and combined with the Bravais lattices this gives 230 space groups. All the space groups are documented in the International Tables for Crystallography.

To understand the basics of diffraction, we have to consider an idealized event, disregarding effects such as absorption and multiple scattering. The lattice is assumed to spread out infinitely and the atoms are regarded as fixed points. When a single X-ray photon or a neutron hits a sample, it can either be absorbed, scattered or pass through the sample. Before the scattering occurs the particle has energy *E*, wave vector ***k***, velocity *v* and wavelength λ:

$$E = \frac{1}{2}mv^2 = \frac{h^2}{2m\lambda^2} \qquad |\boldsymbol{k}| = \frac{2\pi}{\lambda} \qquad \lambda = \frac{h}{mv}$$

Where *h* is Planck's constant and *m* is the mass of the particle. The change of energy for the particle before and after scattering is $\hbar\omega = E_i - E_{fr}$, the scattering vector is $\boldsymbol{Q} = \boldsymbol{k}_i - \boldsymbol{k}_r$ (where the subscripts "i" and "r" mean "incident" and "reflected") and the angle between the initial and final wave vector is 2θ.

Crystal structure can be studied through the superposition of scattered radiation. Nobel laureate W. L. Bragg presented an explanation of crystal diffraction in 1912, the *Bragg law*:

$$2d_{hkl}\sin\theta = n\lambda$$

Where λ is the wavelength of the radiation, θ is the angle of incidence and d_{hkl} is the *interplanar distance.* Braggs law is a consequence of the periodicity of the crystal lattice; the explanation is simple but produces the correct result. The crystal is assumed to be composed by semi-reflecting parallel atomic planes, with an interplanar distance *d*. Each successive plane reflects only a small fraction of the beam. The reflection is specular, *i.e.* the angle of the incident beam to the reflection plane equals the angle of the reflected beam to the same plane. Constructive interference occurs when the path difference is an integral number *n* of wavelengths (see ***Figure 3-2***).

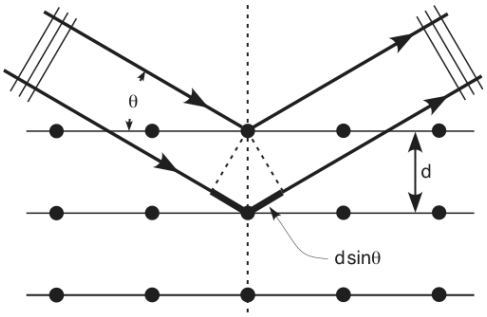

***Figure 3-2**: Beams reflected by parallel crystal planes.*

Periodicity of the atoms creates an ideal situation for the use of Fourier analysis; the mathematical description of the atom distribution can be expanded in a periodic Fourier series in three dimensions. The lattice basis vectors ***a***, ***b*** and ***c*** can be transformed into Fourier-space, and is then called the *reciprocal* lattice basis vectors ***a****, ***b**** and ***c****. The scattering amplitude *F* is proportional to the difference in phase factors of the incident and the reflected beam, and the intensity is proportional to the square of the scattering amplitude. This factor is only non-zero when the difference in the wave vector, ***Q***, equals a reciprocal lattice vector ***G*** of the form $\boldsymbol{G} = h\boldsymbol{a}^* + k\boldsymbol{b}^* + l\boldsymbol{c}^*$. The net result, $\boldsymbol{Q} = \boldsymbol{G}$ is called the *Laue* equation, and is essentially the same expression as the Bragg law. From the Laue equation it is more evident that a diffraction pattern is a function of the scattering vector ***Q*** and that it is a map of the reciprocal space.

When the Laue condition is satisfied, the scattering amplitude from a crystal of *N* cells may be written as $F(\boldsymbol{Q}) = NS(\boldsymbol{Q})$, where *S*(***Q***) is called the *structure factor* and is an integral over a single unit cell. The structure factor can be expressed as a Fourier series:

$$S(\boldsymbol{Q}) \propto \sum_j f_j e^{2\pi i(hx_j + ky_j + lz_j)}$$

Where f_j is a scattering factor dependent on the type of interaction between the probe and the sample, and x_j, y_j, z_j is the fractional coordinates of atom *j*. The intensity of a reflection is proportional to the square of scattering amplitude, so it is also proportional to the square of the structure factor. As seen from the formula of the scattering factor, the intensity of a reflection is then determined by the kind of atoms and their position. In addition, lattice symmetry such as lattice centering causes certain reflections to be extinct. To sum up, only selected directions, determined by the unit cell dimensions and the lattice symmetry, will show scattering intensity, forming a unique diffraction pattern for each crystalline compound. From this pattern, information about crystal structure and lattice parameters can be gained.

Diffraction patterns can be obtained from single crystals, but it is in many cases considerably difficult or even impossible to obtain a single crystal large enough for diffraction measurements. Instead, the most commonly used technique is *powder diffraction.* Ideally, the distribution of the directions of the small crystallites is uniform in a powdered sample. Scattering of the radiation by the crystal planes will then result in cones of scattered intensity.

3.2.1.2 X-ray powder diffraction (XRD)

X-ray photons are scattered by the electron clouds of the atoms, hence X-ray diffraction gives information about the electron density distribution of the material and only probes the average structure. The structure factor for X-ray scattering is dependent of the *form factor f*(***Q***), which increases with increasing *Z*. Instruments for XRD are readily available in laboratory environments and are a widely used source of information about structure, phase purity and interatomic distances.

The basic components of an X-ray diffractometer are: X-ray tube, sample holder and X-ray detector. ***Figure 3-3*** shows the Bruker AXS D8 advanced diffractometer used for analysis in this project. X-rays generated by the cathode tube is of a wavelength characteristic to the target material. The Bruker AXS D8 advance uses a Cu $K_{\alpha 1}$ radiation with a wavelength of 1.54056 Å, it is also common to use a mixture of Cu $K_{\alpha 1}$ and Cu $K_{\alpha 2}$ radiation with an average wavelength of 1.5418 Å. In the diffraction experiment, the radiation is collimated and directed towards the sample, as the sample and the detector are rotated and the intensity of the reflected X-rays is recorded. When the incident and reflecting beam fulfills the Bragg condition, constructive interference will occur and result in a peak in intensity at that angle. The output from the diffractometer is counts per time vs. angle between incident and diffracted beams. Common sample geometry for XRD is a circular flat surface. This surface can be rotated to minimize the effect of non-uniform size and distribution of the crystallites.

Figure 3-3*: Bruker AXL D8 Advance Powder X-ray diffractometer.*

3.2.1.3 Neutron powder diffraction

Neutrons are scattered by nuclei. The structure factor for neutrons scattered by nuclei is dependent on the *scattering length b* which, unlike the form factor for X-ray scattering, is independent of the momentum transfer ***Q***. Since neutrons carry a magnetic moment they can be used to probe magnetic structure through interactions with unpaired electrons. This interaction produces specific Bragg peaks in the scattered spectrum. Almost all materials are coherent scatters, however, vanadium scatters almost completely incoherently. Hence, it is frequently used to make sample containers for powder diffraction. On the other hand, if a sample contains V and it is desirable to find the atomic positions, then this is difficult.

Bragg peaks from neutron scattering can be used to analyze the average structure of the material. Information about local order, vacancies, interstitials *etc.* can be gained through analysis of the total scattering, *i.e.* both the Bragg peaks and the diffuse scattering in between them. The materials in this project were analyzed by neutron time-of-flight (TOF) diffraction By the Polaris instrument at the ISIS facility in U.K. In the experimental setup, seen in ***Figure 3-4***, a polychromatic neutron beam is directed towards the sample and the incident and transmitted neutron flux is monitored. A powdered sample is placed in a cylinder of *e.g.* vanadium, and mounted in a position where it is surrounded by detector banks. The position and time when the scattered neutron hits the detector is recorded. Since the distance from the initial position to the sample and from the sample to the detector is known, the momentum transfer can be determined.

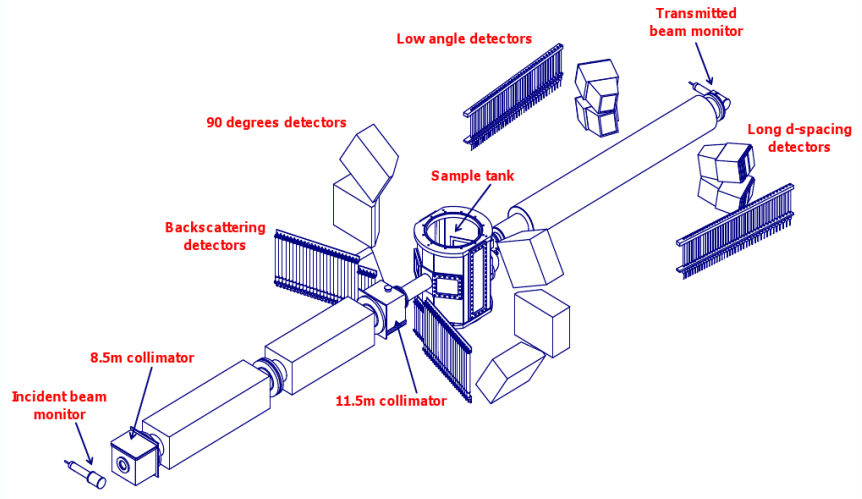

Figure 3-4*: Schematic of the Polaris instrument.*

3.2.1.4 X-ray vs. neutron diffraction

X-ray diffraction is a powerful, non-destructive analysis technique and has the great advantage of being readily accessible since X-ray photons can be generated by a cathode tube. Neutrons, on the other hand, are generated by a nuclear reactor or a spallation source. Hence, neutron diffraction is only available at such large scale facilities. Nevertheless, in some situations invaluable new information can be gained by neutron diffraction. This is due to the different nature of the interactions of neutrons and X-rays with the probed sample. X-rays are scattered by the electron cloud, and hence provide information about the electron density distribution, whereas neutrons are scattered by the nuclei and give nuclear positions. Neutron data gives the bond length between the nuclei, while X-ray diffraction is affected by the electron clouds and so gives a shorter bond-length. Only a small volume close to the surface of the sample is probed in X-ray diffraction. In contrast, neutrons penetrate deep into the sample and provide structural information representative of the bulk. Also, neutrons can probe the magnetic structure of a material. As an example, high-resolution time-of-flight neutron diffraction was used to observe splitting of the magnetic diffraction maxima, revealing the cycloid ordering of the spin configuration of $BiFeO_3$[37].

For X-rays, the scattering value of $f(\boldsymbol{Q})$ is proportional to the number of electrons and hence to the atomic number Z. This means that some lighter elements cannot be "seen" by X-ray diffraction. Elements that are close to each other in the periodic table are hard to distinguish. Neutrons, on the other hand, show no simple relationship between the scattering length and the atomic number. Therefore, it can be used to detect light atoms (*e.g.* H, C, N and O) in the presence of heavy atoms and distinguish between atoms with similar Z. Neutron scattering also depends on the isotope whereas X-ray diffraction does not. For example, neutron diffraction can distinguish between the isotopes H and D. Still, there are situations when identifying atoms with neutron diffraction is challenging because of the high absorption of neutrons in the material. The absorption varies widely with the atomic number Z, examples of elements with high absorption cross area are Li, B, Cd, Gd, Sm and Eu.

3.2.2 Structure model refining

Information about atomic scale structure can be gained through diffraction techniques using neutron or X-ray radiation. Single crystal diffraction gives a set of separate data which can be analyzed by Fourier methods. Unfortunately, large single crystals can be very difficult and sometimes impossible to produce. Even if there is no single crystal sample of a compound, polycrystalline powdered samples are much more easily attainable. The diffraction peaks from a powdered sample grossly overlap, which makes the structural analysis of the pattern difficult. Hugo Rietveld (***Figure 3-5***)developed computer-based procedures to analyze the full information gained from powder diffraction.[56] The *Rietveld method* has made it possible today to routinely make accurate refinements of structure from powder diffraction data[57]. In this project, the software GSAS[58] was used for structure refinement.

Figure 3-5: *Dr. Rietveld at the neutron powder diffractometer at the High Flux Reactor of the Energy Research Foundation ECN in Petten, the Netherlands. (1987).*

The analysis process of the Rietveld method makes use of least-squares refinements to obtain the best fit between observed intensities and the intensities calculated from the simultaneously refined models. Here, solid solutions of compounds with known crystal structure have an advantage, since the structure of the parent compounds can be used as a starting point. It is important to notice that the Rietveld method is not a structural solution method, but a structure refinement method. If the initial guess of the structure model is not chemically sound, it is impossible to determine an accurate model by refining.

Diffracted intensities are recorded as a function of scattering angle 2θ for X-ray diffraction and of time-of-flight for neutrons. At each increment *i* the observed intensity value is denoted y_i. The intensity calculated by the model is denoted y_{ic} and the residual at the *i*th step is $(y_i - y_{ic})$. The quantity to be minimized by the least-squares refinement is the sum of the weighted squared residuals over all steps *i*:

$$\sum_i w_i (y_i - y_{ic})^2$$

Where $w_i = 1/y_i$ and y_{ic} is calculated from a number of factors obtained from the models including: the value of the squared structure factor (since the intensity is proportional to this value), the intensity contribution from the background, preferred orientation and Lorentz, polarization, multiplicity and absorption factors. To judge the quality of the fit reliability factors, "R-values", are calculated. Common R-values are "R-structure factor" (R_F), "R-Bragg" (R_B), "R-expected" (R_e) and "R-weighted pattern"(R_{wp}):

$$R_F = \frac{\sum\left|\sqrt{I_{hkl}} - \sqrt{I_{hkl,c}}\right|}{\sum\sqrt{I_{hkl}}}$$

$$R_B = \frac{\sum\left|I_{hkl} - I_{hkl,c}\right|}{\sum I_{hkl}}$$

$$R_e = \left(\frac{N-P}{\sum w_i {y_i}^2}\right)^{1/2}$$

$$R_{wp} = \left(\frac{\sum w_i\left(y_i - y_{i,c}\right)^2}{\sum w_i {y_i}^2}\right)^{1/2}$$

where I_{hkl} is the observed intensity and $I_{hkl,c}$ is the calculated intensity of the *h k l* Bragg reflection at the end of the refinement cycle. N is the number of observed terms used and P is the number of parameters being refined. R-Bragg and R-structure factor values are useful because they do not get influenced my misfits that do not involve Bragg-peaks. However, they are biased in favor of the model. The R-factor that best reflects the progress of the refinement is instead R_{wp}. Another useful value is the "goodness of fit", χ^2:

$$\chi^2 = \left(\frac{R_{wp}}{R_e}\right)^2$$

The goodness of fit should be 1 or just slightly above. If χ^2 value is around 2 or higher, it is a warning that your model is inadequate. A value lower than 1 does not indicate a good fit, but that the model has more parameters than justified by the quality of the data. All indicators of the fit of the model to the data must be considered based on chemical and mathematical knowledge; they are not indicators to whether or not the model is *true*, but mere tools to aid the judgment.

3.2.3 Magnetism and magnetization measurements

A material with a macroscopic magnetic field is called ferromagnetic[22]. The field is generated by unpaired electrons that align their magnetic moments in a parallel manner. Unpaired electrons can also order in ferri- and antiferromagnetic structures. In an antiferromagnetic phase, the spins are aligned opposite to each other, resulting in a zero net field. Ferrimagnetic order is also antiparallel, however, the magnitudes of the opposing spins are unequal and hence a macroscopic magnetic field remains. The magnetic ordering only exists below a critical temperature, for ferro- and ferrimagnets this temperature is called the Curié temperature T_C, and for antiferromagnetic materials it is called the Néel temperature T_N. Above these temperatures the materials are paramagnetic.

When a magnetic field is applied to a material, *magnetization* of the substance will occur. Spins of the unpaired electrons of a ferromagnetic material can be aligned with an applied field, and when the field is removed the material itself will still be magnetized and have a macroscopic magnetic field. This will cause a hysteresis loop if the *magnetization M* is plotted against the *applied field H* and this hysteresis loop that is characteristic for ferromagnetic materials. The degree of magnetization, *i.e.* the response of a material to an applied magnetic field, can be described by the *magnetic susceptibility* χ:

$$\chi = \frac{M}{H}$$

The magnetic susceptibility as a function of temperature behaves differently for materials with different "ferroic" ordering. Ferro and ferrielectric materials have a susceptibility that decreases with increasing temperature while the susceptibility of an antiferromagnetic material increase with increasing temperature. To investigate magnetic susceptibility, the magnetization caused by an applied magnetic field is measured and plotted as a function of either temperature, change in applied field or time. Magnetization of a sample can be measured in a couple of different units, commonly used units are emu/g, emu/cm^{-3} and A/m. If the number of atoms in the sample can be estimated, the magnetic moment per atom expressed in Bohr magnetons μ_B can be calculated. The unit of the applied magnetic field can be Oe, Gauss or A/m. The denomination emu is an abbreviation for "electromagnetic units" and is used in the *centimetre gram second system of units* (cgs) and the relation to the *International System of units* (SI) is $1\mathrm{emu} = 1 \times 10^{-4}\mathrm{Am}$. Oe and Gauss are both cgs units and are related to SI unit as $1Oe \approx 80\ \mathrm{A/m}$ and $1\mathrm{Gauss} = 1 \times 10^{-4}\mathrm{Tesla}$. In this project, measurements of magnetization were carried out on a commercial Superconducting Quantum Interference Device (SQUID) magnetometer from Quantum Design.

4 Experiments

4.1 Solid solution series

Powdered polycrystalline samples of xBiMO$_3$-(1-x) ATiO$_3$ (M = Cr or Fe; A = Ba or Sr; x = 0, 0.2, 0.4, 0.5, 0.6, 0.8 and 1) where synthesized by solid state sintering. The samples were characterized by powder X-ray diffraction.

4.1.1 Synthesis

The start materials used were powders of bismuth oxide (Sigma-Aldrich, 99.99%), titanium dioxide (Aldrich, >99%), chromium(III) oxide (Acros organics, 99%), iron(III) oxide (KEBO, purum), barium carbonate (Merck, >99%) and strontium carbonate (Merck, selectipur). Stochiometric amounts of the powders were mixed and milled in an agate mortar for about 20 minutes, with ethanol added as a milling aid. The powders were calcined for 10 hours in alumina crucibles at temperatures between 600 and 900 °C. Subsequently, the powders were re-milled and pressed into pellets. The pellets were heated for 40 hours and then the cycle was repeated with milling, pelletizing and firing at raised temperatures. ***Table 4-1*** shows the individual sintering temperatures.

Table 4-1: *Sintering temperature and times for the solid solution series.*

compound	x	calc. (°C/h)	SSR1 (°C/h)	SSR2 (°C/h)	compound	x	calc. (°C/h)	SSR1 (°C/h)	SSR2 (°C/h)
xBiFeO$_3$-(1-x)BaTiO$_3$	1.0	600/16	750/40	790/40	xBiFeO$_3$-(1-x)SrTiO$_3$	1.0	600/16	750/40	790/40
	0.8	600/16	840/40	940/40		0.8	600/16	840/40	940/40
	0.6	700/16	840/40	940/40		0.6	700/16	840/40	940/40
	0.5	700/16	900/40	1000/40		0.5	700/16	900/40	1000/40
	0.4	800/16	1000/40	1100/40		0.4	800/16	1000/40	1100/40
	0.2	800/16	1000/40	1100/40		0.2	800/16	1000/40	1100/40
	0.0	900/16	1215/40	1240/40		0.0	900/16	1215/40	1240/40
compound	x	calc. (°C/h)	SSR1 (°C/h)	SSR2 (°C/h)	compound	x	calc. (°C/h)	SSR1 (°C/h)	SSR2 (°C/h)
xBiCrO$_3$-(1-x)BaTiO$_3$	1.0	600/16	750/40	790/40	xBiCrO$_3$-(1-x)SrTiO$_3$	1.0	600/16	750/40	790/40
	0.8	600/16	840/40	940/40		0.8	600/16	840/40	940/40
	0.6	600/16	840/40	940/40		0.6	600/16	840/40	940/40
	0.5	700/16	900/40	1000/40		0.5	700/16	900/40	1000/40
	0.4	800/16	1000/40	1100/40		0.4	800/16	1000/40	1100/40
	0.2	800/16	1000/40	1100/40		0.2	800/16	1000/40	1100/40
	0.0	900/16	1215/40	1240/40		0.0	900/16	1215/40	1240/40

4.1.2 Phase purity and structure

X-ray powder diffraction measurements at room temperature were performed with a *Bruker AXS D8 Advance* diffractometer, using Cu $K_{\alpha 1}$ radiation (λ = 1.54056 Å). Short scans (20 minutes), with a step

size of 0.05°, counting time of 1.11 s/step and a 2θ range of 20°-70° were recorded to investigate the phase purity of all the samples in the series. Longer X-ray diffraction data was collected from the three successfully synthesized solutions with x = 0.5. The measurements had a step size of 0.01°, counting time of 3.9 s/step and a 2θ range of 19°-100° and they were made for subsequent structure model fitting and Rietveld refinement using the GSAS software.

4.2 Focus on 50/50 solid solutions

Polycrystalline powdered samples of $0.5BiFeO_3$-$0.5BaTiO_3$, $0.5BiFeO_3$-$0.5SrTiO_3$, $0.5BiCrO_3$-$0.5BaTiO_3$ and $0.5\ BiCrO_3$-$0.5SrTiO_3$ where synthesized by solid state sintering. The powders were characterized by X-ray diffraction, neutron time-of-flight data and magnetization measurements. Structural models where refined by the Rietveld least-squares minimization method, using the GSAS[58] software.

4.2.1 Synthesis

The samples were prepared from powders of bismuth oxide (Aldrich, 99.999%), titanium dioxide (Aldrich, 99.8%), chromium(III) oxide (Sigma-Aldrich, >98%), iron(III) oxide (Alfa Aesar, 99.998%), barium carbonate (Aldrich, 99.98%) and strontium carbonate (Aldrich, >99.9%). Stochiometric amounts of the reactants were mixed and milled with ethanol in a Pulverisette 7 ball mill using teflon milling houses and zirconia milling balls, 3x20 minutes at 400 rpm. The dry powders were calcined at 700 °C for 16 h and subsequently sintered two times, once at 900 °C and once at 1000 °C for 40 h, with intermediate ball-milling and compacting.

4.2.2 Diffraction data collection

X-ray powder diffraction measurements at room temperature were performed with a *Bruker advanced D8* diffractometer, using CuK_α radiation (λ = 1.54056Å). Short scans (20 minutes), with a step size of 0.05°, counting time of 1.11 s/step and a 2θ range of 20°-70° were recorded to investigate the phase purity of all the samples in the series. Longer scans (10 h) of higher quality, with a step size of 0.01°, counting time of 3.9 s/step and a 2θ range of 19°-100° were made for subsequent structure model fitting and Rietveld refinement using the GSAS software.

Neutron time-of-flight diffraction data were collected from the polycrystalline powdered samples using the Polaris diffractometer at the ISIS pulsed spallation source, Rutherford Appleton Laboratories, UK[59]. The data used was collected by the backscattering detector bank, scattering angles 130° < 2θ < 160° corresponding to a *d*-range of 0.2 < d[Å] <3.2 and with a resolution of $\Delta d/d \approx 5 \times 10^{-3}$. A thin-walled cylindrical vanadium can with 6 mm diameter was used as a sample holder. Neutron scattering was measured for 10h at ambient conditions

Long-range, time averaged structure models were refined by the Rietveld least-squares minimization method using the GSAS software. A cubic model with space group $Pm\bar{3}m$ with the Bi^{3+} and *A* (*A* = Ba^{2+} or Sr^{2+}) ions at the 1(*a*) site (0, 0, 0), the Ti^{4+} and *M* (*M* = Fe^{3+} or Cr^{3+}) at the 1(*b*) site (½, ½, ½) and the O^{2-} at the 3(*c*) sites (0, ½, ½ etc.) was fitted to the diffraction data. The refined parameters was: a scale factor, cubic lattice parameter *a*, isotropic thermal vibration factors for each atomic site (u_A, u_B, u_O), 16 coefficients of a shifted Chebyshev polynomial describing the background scattering and 3 coefficients describing Gaussian and Lorentzian contributions to the Bragg peak profiles.

4.3 Complementary samples with high bismuth content

Complementary samples $BiFeO_3$-$BiCrO_3$, $BiFeO_3$-$BiMnO_3$ and $BiCrO_3$-$BiMnO_3$ were prepared by solid state sintering from powders of bismuth oxide (Sigma-Aldrich, 99.99%), titanium dioxide (Aldrich, >99%), chromium(III) oxide (Acros organics, 99%), iron(III) oxide (KEBO, purum), barium carbonate (Merck, >99%), strontium carbonate (Merck, selectipur) and manganese oxide (Aldrich, 99%). The experimental synthesis procedure was as described for the solid solutions series, with firing temperatures of 600 °C, 750 °C and 790 °C.

4.4 Magnetization measurements

Magnetization measurements were performed by Roland Mathieu at Uppsala University, using a Quantum Design SQUID MPMS XL magnetometer. The samples were cooled in zero magnetic field and then the magnetization in a small field was measured while the temperature was increased and decreased. Also, magnetization *M* was recorded as a function of applied field *H* at low temperature (5 K). The magnetic measurements were carried out on the two successfully made 50/50 solutions with the highest purity, $0.5BiFeO_3$-$0.5BaTiO_3$ and $0.5BiCrO_3$-$0.5SrTiO_3$.

5 Results and discussion

5.1 Synthesis, structure and solution limits of the solid solution series

Pure $BiFeO_3$ and $BiCrO_3$ were not successfully synthesized by the solid state sintering route. The series xBiFeO$_3$-(1-x)BaTiO$_3$ (***Figure 2-1***) and xBiFeO$_3$-(1-x)SrTiO$_3$ (***Figure 5-2***) showed solid solubility over $0.2 < x < 0.8$. X-ray diffraction data indicated a cubic perovskite structure for all successfully synthesized samples, but for xBiFeO$_3$-(1-x)SrTiO$_3$, x = 0.8, the peaks looks like they are about to split, indicating rhombohedral structure. The xBiCrO$_3$-(1-x)BaTiO$_3$ series did not form solid solutions for any x investigated by the solid state sintering route (***Figure 5-3***). However, the xBiCrO$_3$-(1-x)SrTiO$_3$ series showed solid solubility for x = 0.2, 0.4, 0.5 (***Figure 5-4***). A cubic perovskite model fitted the diffraction data.

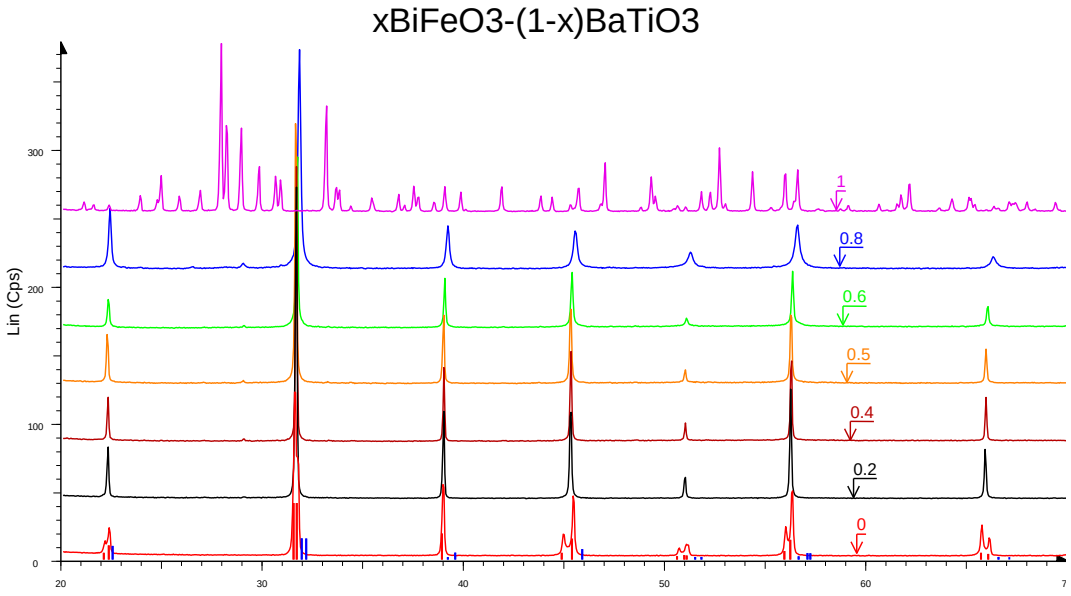

Figure 5-1: *Powder-X-ray diffractogram for xBiFeO$_3$ - (1-x)BaTiO$_3$, x = 0, 0.2, 0.4, 0.5, 0.6, 0.8, and 1.*

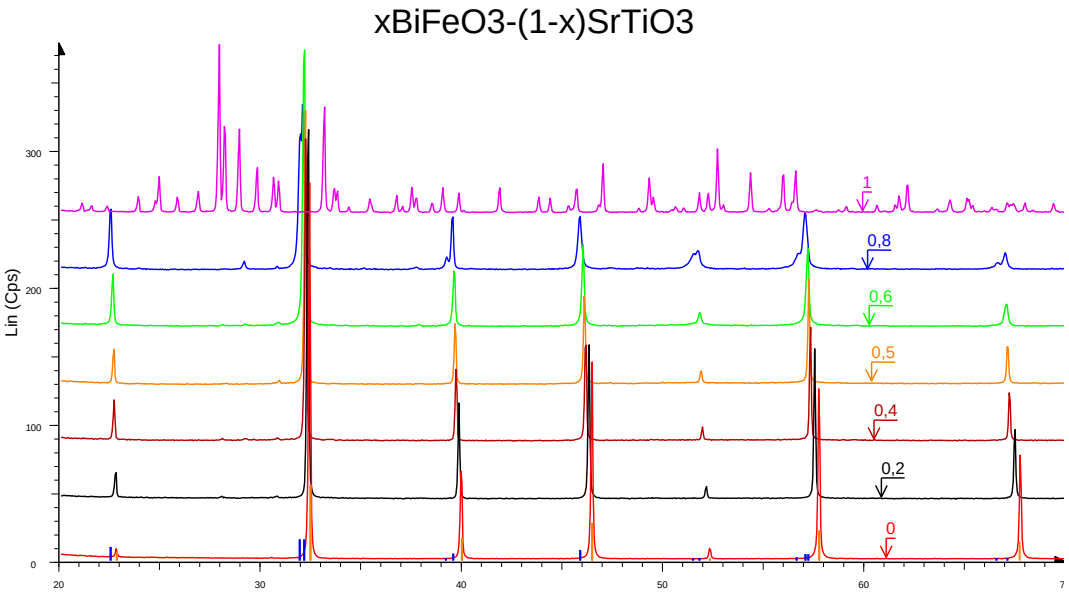

Figure 5-2: *Powder-X-ray diffractogram for $xBiFeO_3$ - (1-x)$SrTiO_3$, x = 0, 0.2, 0.4, 0.5, 0.6, 0.8, and 1.*

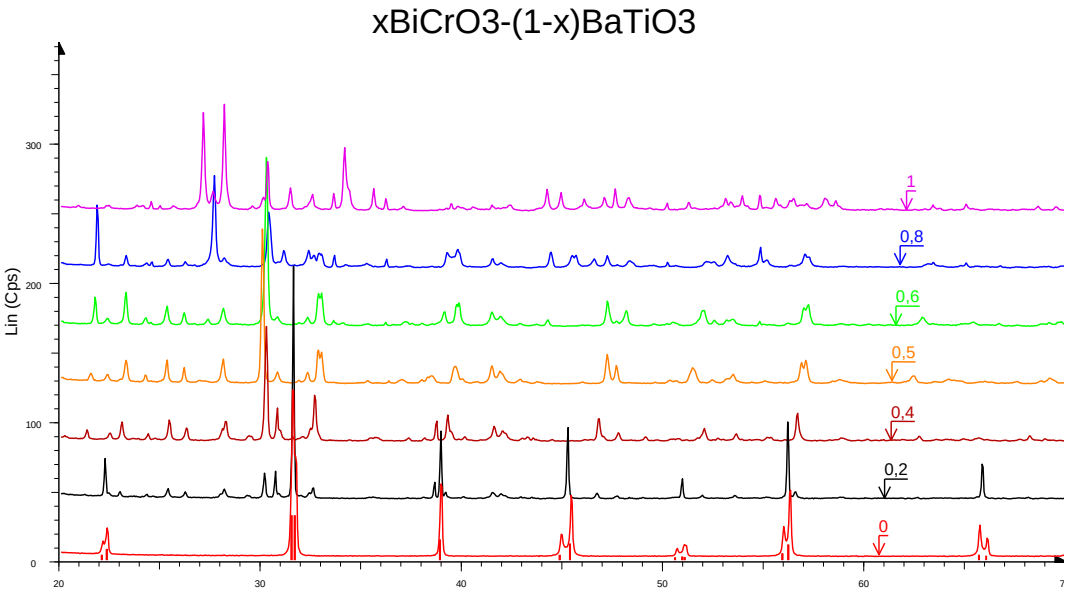

Figure 5-3: *Powder-X-ray diffractogram for $xBiCrO_3$ - (1-x)$BaTiO_3$, x = 0, 0.2, 0.4, 0.5, 0.6, 0.8, and 1.*

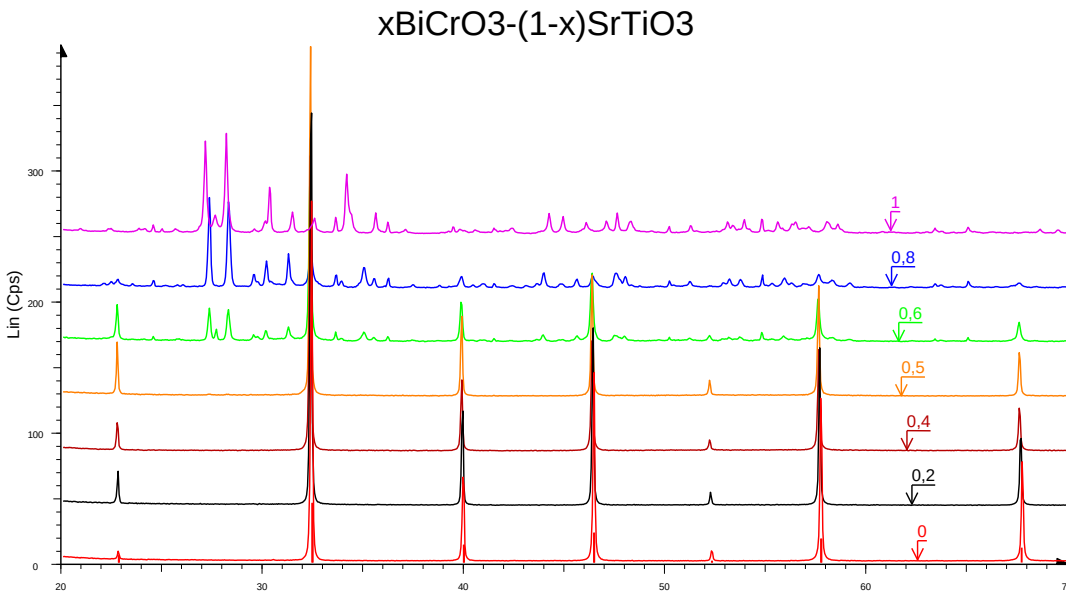

Figure 5-4: *Powder-X-ray diffractogram for $xBiCrO_3$ - $(1-x)SrTiO_3$, x = 0, 0.2, 0.4, 0.5, 0.6, 0.8, and 1.*

Lattice parameter, *a,* for the solid solution series was calculated using the Celref software and cubic structure model with space group $Pm\bar{3}m$ (see ***Figure 5-5***). The trends can be explained by the ionic radii of the *A*- and *B*-site ions, see ***Table 5-1***. When substituting $BaTiO_3$ into $BiFeO_3$, the cell parameter increases with increasing amount of $BaTiO_3$, which is in accordance with Ba^{2+} having a larger ionic radius than Bi^{3+}. For the next trend, we see that increasing amount of $SrTiO_3$ in $BiFeO_3$ decreases the lattice parameter. This can be explained if iron is in high-spin configuration, then substituting Bi^{3+} and Fe^{3+} for the smaller Sr^{2+} and Ti^{4+} would result in a smaller unit cell. The lattice parameter for $x BiCrO_3$-$(1-x)SrTiO_3$, where $0.2 < x < 0.5$, is almost constant, which is consistent with the similar ionic radii of the corresponding ions. It should be pointed out that for $0.8BiFeO_3$-$0.2SrTiO_3$ it is doubtful that the structure actually is cubic. However, the data was not good enough for Celref to handle a rhombohedral fitting. To get an idea of the consistency of the Celref lattice parameter refinements, higher quality X-ray data was collected from the three successfully sintered samples with $x = 0.5$ and the same cubic model was refined by the GSAS software. The results correspond well, as seen in ***Table 5-2***.

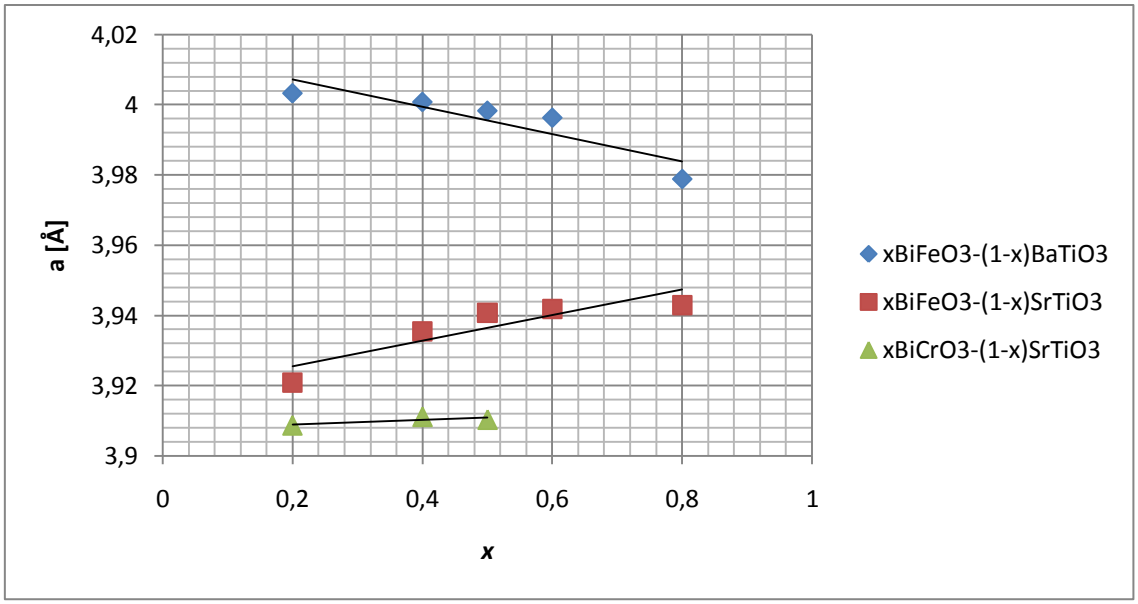

Figure 5-5: *Fitted lattice parameter for the solid solution series*

Table 5-1: *Ionic radii, from R. D. Shannon, Acta Crystallographica (1976) A32 75, except Bi^{3+}, for which the value is extrapolated. Ionic radii of both high-spin (HS) and low-spin (LS) configuration of Fe^{3+} is reported.*

ion	radius (Å)	CN
Fe^{3+} LS	0.55	6
Fe^{3+} HS	0.645	6
Cr^{3+}	0.615	6
Ti^{4+}	0.605	6
Ba^{2+}	1.61	12
Sr^{2+}	1.44	12
Bi^{3+}	1.17	12

Table 5-2: *Comparison of lattice parameter a for the x = 0.5 samples, refined by the Celref and GSAS softwares.*

Compound, x = 0.5	celref	GSAS
$BiFeO_3$-$BaTiO_3$	3.9983	3.99942(8)
$BiFeO_3$-$SrTiO_3$	3.9408	3.94101(5)
$BiCrO_3$-$SrTiO_3$	3.9103	3.91133(5)

It is should be noticed that the synthesis of $x$$BiFeO_3$ - (1-x)$BaTiO_3$ for high x seems to be sensitive to factors that are not explicitly identified. This is evident from an attempt to reproduce the x = 0.8 sample; equivalent procedure and the same equipment was used as for the first sample, but the oxides and carbonates were of higher purity than the reactants used for the previous sample. XRD

scans (using the same parameter file) from the synthesis can be seen in ***Figure 5-6***. The structure of the first samples (***Figure 5-1***) is clearly cubic, while the reproduced sample shows a distinct separation into double peaks, indicating rhombohedral structure. These differing results from solid state sintering are also supported by reports in the literature. Kumar *et al.*[45] report a rhombohedral structure for x = 0.7 (maximum sintering temperature 940 °C) while Buscaglia *et al.*[60] report a cubic structure for the same x (maximum sintering temperature 900 °C). Ianculescu *et al.*[46] report the gradual change from rhombohedral structure at x = 1 to cubic structure at x = 0.7 (maximum sintering temperature 800 °C) and Yoneda *et al.*[61] report rhombohedral structure for x = 0.75 and cubic for x = 0.6. Factors that may influence the formation of the compounds is bismuth evaporation and the occurrence of meta-stable polymorphs of bismuth oxide. Bismuth evaporation in turn, is dependent on sintering temperatures, sintering times and maybe also of sample compacting before calcinations. It is clear that the complete process of formation of the compounds with high bismuth content is not explicitly known, and that the factors influencing the sintering need to be further investigated.

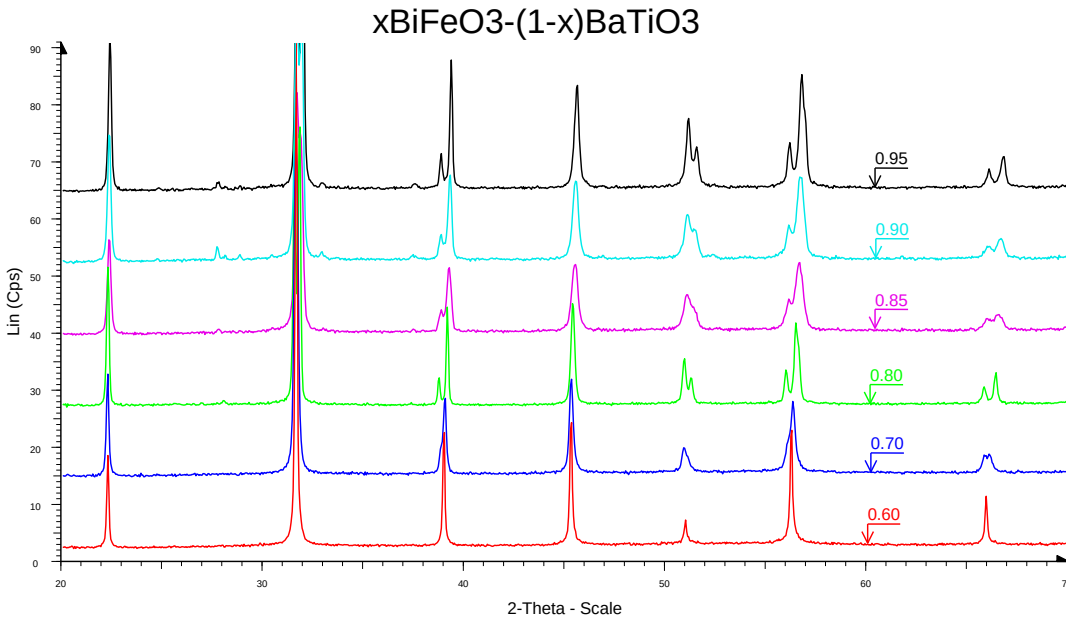

Figure 5-6: *Samples of $xBiFeO_3$ – (1-x) $BaTiO_3$ (x = 0.6, 0.7, 0.80, 0.85, 0.9, and 0.95)*

5.2 Synthesis and structure of the 50/50 samples

The XRD scans of the 50/50 samples (x = 0.5) can be seen in (***Figure 5-7***), where it can be seen that the synthesis of $0.5BiCrO_3$ – $0.5BaTiO_3$ was unsuccessful. The other three samples seem to possess a cubic structure. Subsequent neutron TOF data revealed several impurities in $0.5BiFeO_3$ – $SrTiO_3$ and consequently the subsequent GSAS refining results is not reported, neither was this sample sent for magnetization measurements.

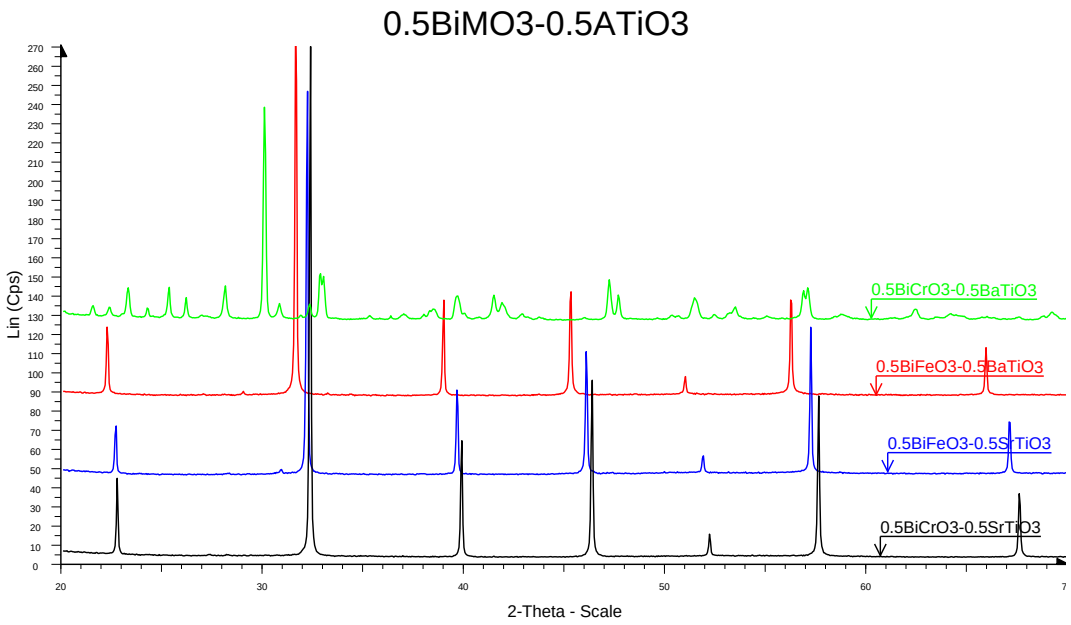

Figure 5-7: *Powder X-ray diffractogram for 0.5$BiFeO_3$ - 0.5$BaTiO_3$, 0.5$BiFeO_3$ – 0.5$SrTiO_3$, 0.5$BiCrO_3$ – 0.5$BaTiO_3$ and 0.5 $BiCrO_3$ – 0.5$SrTiO_3$ (0.5$BiMO_3$ – 0.5$ATiO_3$, M = Fe or Cr, Mn; A = Ba or Sr).*

Neutron TOF data and the refined models are displayed in ***Figure 5-8*** for $BiFeO_3$ – $BaTiO_3$ and in ***Figure 5-9*** for $BiCrO_3$ – $SrTiO_3$. From XRD data, the structure of the compounds looks similar (cubic), but when looking closely at the neutron data, one can see that some of the peaks apparent for $BiFeO_3$ – $BaTiO_3$ seems very small or even disappear for $BiCrO_3$ – $SrTiO_3$. This is due to the scattering factor of chromium and titanium, b_{Cr} = 3.635 and b_{Ti} = -3.438, which almost cancels out the reflections from the *B*-site. This fact might seem discouraging, but local structural information from the interesting *A*-site can still be gained from the data.

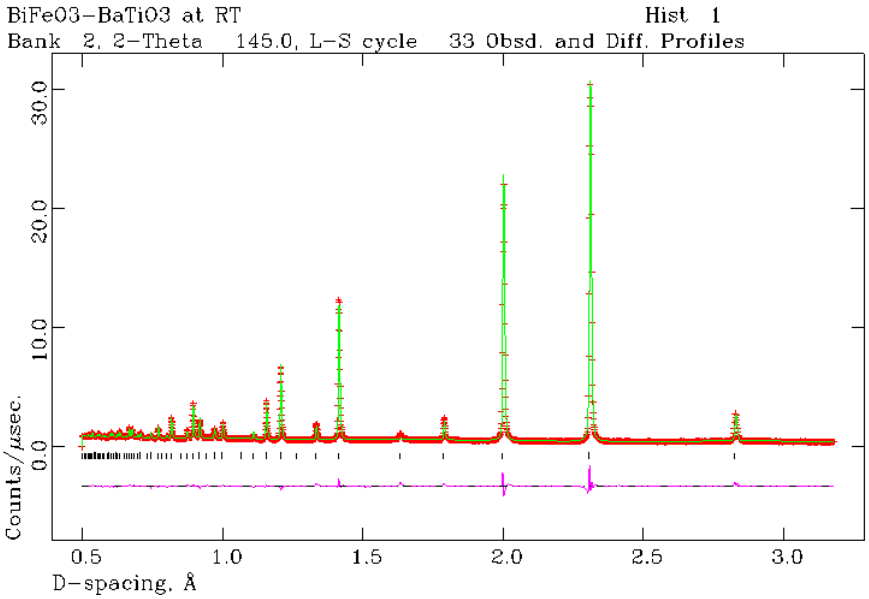

Figure 5-8: *Neutron TOF data and refined model for $BiFeO_3$-$BaTiO_3$. The red crosses indicate measured counts, the green line is the refined model and the pink line below indicates the difference between the observed and calculated pattern. The short vertical lines in between marks the Bragg reflexes.*

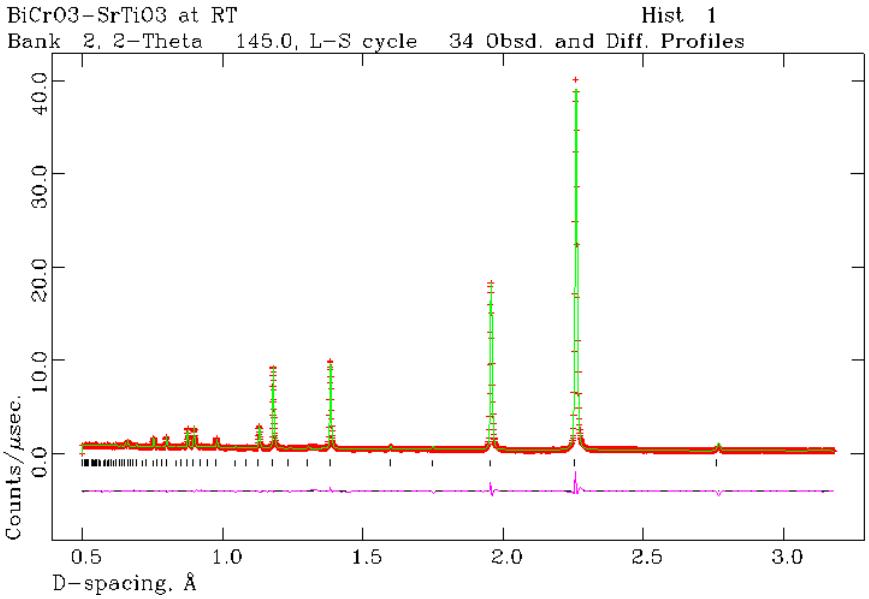

Figure 5-9: *Neutron TOF data and refined model for $BiCrO_3$-$SrTiO_3$. The red crosses indicate measured counts, the green line is the refined model and the pink line below indicates the difference between the observed and calculated pattern. The short vertical lines in between marks the Bragg reflexes.*

Lattice parameter, cell volume and isotropic thermal vibration factors for the *A-, B- and* O- sites gained from the GSAS refining of the neutron TOF data are reported in ***Table 5-3***. Here, data from the samples $BiMnO_3$ – $BaTiO_3$ and Bi MnO_3 – $SrTiO_3$ from the article by Norberg *et al.*[16] are included for comparison. Bond distances determined by the refinement are given in ***Table 5-4***.

Table 5-3: *Parameters gained from Rietveld refining of neutron TOF data. A cubic model with space group $Pm\bar{3}m$ was used.*

Sample	Lattice parameter, a [Å]	Cell volume [Å^3]	u_{isoA} [Å^2]	u_{isoB} [Å^2]	u_{isoO} [Å^2]
$BiFeO_3$-$BaTiO_3$	4.001085(26)	64.0520(10)	0.0737(8)	0.01410(3)	0.01191(11)
$BiCrO_3$-$SrTiO_3$	3.912457(27)	59.8890(10)	0.0209(4)	0.003(6)	0.02553(21)
$BiMnO_3$-$BaTiO_3$[*]	3.99366(2)	63.6960(10)	0.0497(3)	0.00705(18)	0.02449(13)
$BiMnO_3$-$SrTiO_3$[*]	3.92972(3)	60.6390(10)	0.0236(3)	0.0048(2)	0.0396(3)
$BaTiO_3$[†]		64.2100(10)	0.00345(9)	0.00518(14)	

[*]Samples from Norberg et al.[16].
[†]Reference sample, data refined by Stefan Norberg.

Table 5-4: *Bond distances, calculated from a refined cubic model (space group $Pm\bar{3}m$) fitted to neutron TOF data. A and B in the table indicates the sites in the perovskite structure.*

Sample	*A*-O[Å]	*B*-O[Å]	*A*-*B*[Å]
$BiFeO_3$-$BaTiO_3$	2.829190(10)	2.000540(10)	3.465040(20)
$BiCrO_3$-$SrTiO_3$	2.766520(10)	1.956230(10)	3.388290(20)

In the article by Norberg *et al.,* it is pointed out that the high thermal vibration factor for the *A*-site indicates disorder, and RMC analysis of the neutron TOF data shows that the Bi^{3+} ion has a off center location within the oxygen cuboctahedra, favored by the lone-pair electrons. In comparison, $BiCrO_3$-$SrTiO_3$ has a thermal vibration factor of the *A*-site in the same order of magnitude, and even a bit larger for $BiCrO_3$-$SrTiO_3$. These numbers should be compared with the much lower value for the $BaTiO_3$ reference sample. The thermal vibration factors implies local disorder and motivates RMC analysis of total neutron scattering data, since the Rietveld refinement of the Bragg peaks only provides information about the average structure.

5.3 Synthesis outcome of the samples with high bismuth content

X-ray diffraction data from the attempted synthesis of $BiFeO_3$-$BiCrO_3$, $BiFeO_3$-$BiMnO_3$ and $BiCrO_3$-$BiMnO_3$ is seen in ***Figure 5-10***. No phase pure solid solutions were produced by the solid state sintering route. The results are in accordance with the unsuccessful synthesis of $BiFeO_3$ and $BiCrO_3$ and other synthesis routes may yield a different result.

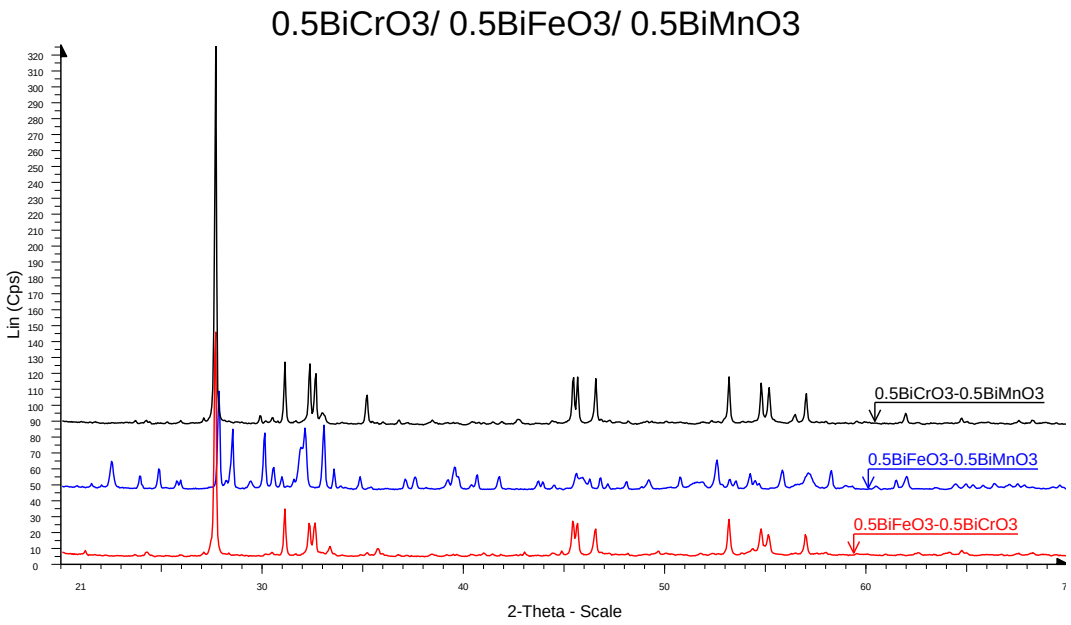

Figure 5-10: *Powder X-ray diffractogram for the complementary samples $BiFeO_3$-$BiCrO_3$, $BiFeO_3$-$BiMnO_3$, $BiCrO_3$-$BiMnO_3$.*

5.4 Results of magnetization measurements

The temperature dependence of the zero-field-cooled (ZFC)/field-cooled (FC) magnetization (***Figure 5-11***) shows an antiferromagnetic transition for $BiCrO_3$ – $SrTiO_3$ (turquoise line) at 10K, and a paramagnetic behavior at temperatures above. The $BiFeO_3$ – $BaTiO_3$ (black line) and $BiFeO_3$ - $SrTiO_3$ (dark blue line) samples prepared by Sergey Ivanov (Karpov Institute, Moscow) might have an antiferromagnetic transition around 200K. In contrast, the $BiFeO_3$ – $BaTiO_3$ sample prepared in this project seems to be ferromagnetic (the hysteresis loop can be seen in ***Figure 5-12***) with a Curie temperature above 400K (which is the highest temperature measured). However, it is hard to say whether this is an intrinsic or extrinsic effect.

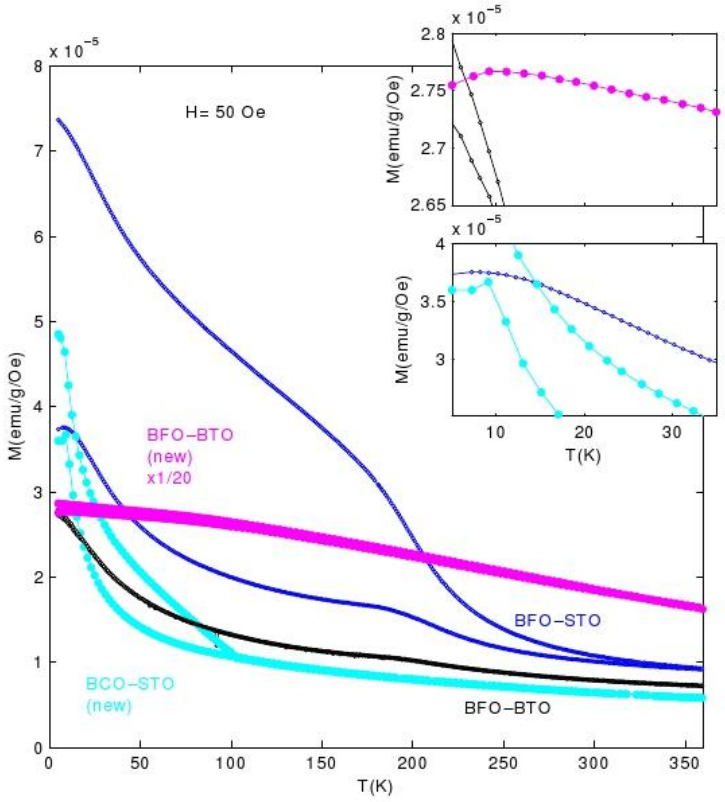

Figure 5-11: *The temperature (T) dependence of the zero-field-cooled/ field-cooled magnetization (M), performed by Roland Mathieu, Uppsala University, Sweden. The black and dark blue line represents $BiFeO_3$ – $BaTiO_3$ and $BiFeO_3$ – $SrTiO_3$ samples previously prepared by Sergey Ivanov. The pink line indicates the measurements of the $0.5BiFeO_3$ – $BaTiO_3$ sample, and the turquoise line the $BiCrO_3$- $SrTiO_3$ sample. The insets are magnifications of the data at low temperatures.*

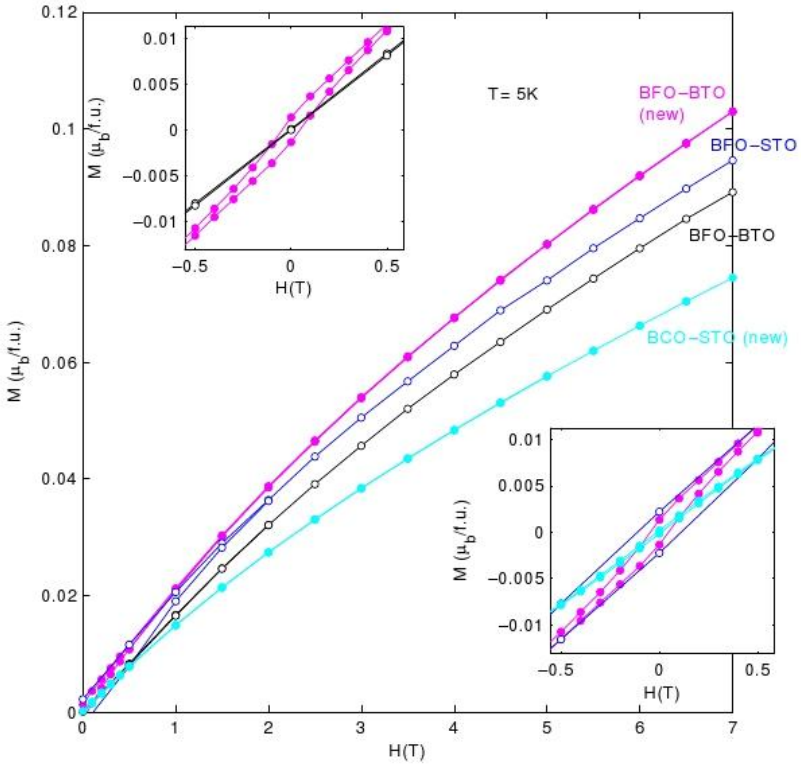

***Figure 5-12**:The magnetic field (H) dependence of magnetization (M) at 5K, measured by Roland Mathieu at Uppsala University, Sweden. The black and dark blue line represents $BiFeO_3$ – $BaTiO_3$ and $BiFeO_3$ – $SrTiO_3$ samples previously prepared by Sergey Ivanov. The pink line indicates the measurements of the $0.5BiFeO_3$ – $BaTiO_3$ sample, and the turquoise line the $BiCrO_3$- $SrTiO_3$ sample.*

6 Summary of results and concluding remarks

By solid state sintering, $BiFeO_3$ formed binary solid solutions with both $BaTiO_3$ and $SrTiO_3$ for all compositions attempted and no solution limits were identified. $BiCrO_3$ did not form phase pure solid solutions with $BaTiO_3$ but partially with $SrTiO_3$, with a solution limit between 50 and 60% $BiCrO_3$. All the successfully sintered samples showed a cubic structure, although onset of peak splitting was observed for $0.8BiFeO_3 – 0.2\ SrTiO_3$, indicating a transition to rhombohedral structure. Samples with higher bismuth content were more difficult to synthesize, in accordance with literature reports. Factors affecting the synthesis may include purity of starting materials, contamination of meta-stable phases of bismuth oxide and bismuth evaporation. The high isotropic thermal vibration factors of the *A*-site for $BiFeO_3 – BaTiO_3$ and $BiCrO_3$- $SrTiO_3$ implies disagreement with the average structural model gained from Rietveld refinement, indicates local disorder and motivates further RMC modeling of total neutron scattering. Magnetization measurements showed an antiferromagnetic transition at 10K for $BiCrO_3 – SrTiO_3$ and a ferromagnetic behavior of $BiFeO_3 – BaTiO_3$. However, it is difficult to know whether these are intrinsic or extrinsic effects.

7 Future work

To better understand the local structure, total scattering data can be analyzed by reverse Monte Carlo (RMC) modeling. Other reported methods of probing local non-centrosymmetry that could be complementary are Raman and IR-spectroscopy [46,60]. The magnetic order and properties can be confirmed and predicted for new materials by applying Density Function Theory (DFT) calculations on the solid solution series.

In this project, the magnetic properties of the compounds have been analyzed. Since the goal is to find magnetoelectric materials, it is of course of interest to also study ferroelectric properties and investigate a possible coupling between magnetization and electric polarization. Magnetoelectric coupling can be studied by measuring polarization as a function of an applied magnetic field or magnetization as a function of an applied electric field. However, these measurements are obstructed by high leakage currents. Instead, Schmidt *et al.*[62] measured the magnetocapacitance by impedance spectroscopy on thin films. Another example of analysis of multiferroic properties is Zhao *et al.*[4] who investigated electrical control of antiferromagnetic domains in multiferroic $BiFeO_3$ films at room temperature. Also, the ferroelectric structure was measured using piezo force microscopy, and X-ray photoemission electron microscopy as well as its temperature dependence was used to detect the antiferromagnetic configuration. These are examples of pure $BiFeO_3$, of course, if solid solutions are shown to exhibit multiferroic properties, it would be of highest interest to study the composition dependency of the magnetic, ferroelectric and magnetoelectric properties.

Microstructure, chemical homogeneity and relative grain size, can be studied by Scanning Electron Microscopy (SEM) and Energy Dispersive X-ray fluorescence (EDX) and the effect of the admixture on grain growth could be analyzed. For example, Ianculescu *et al.*[46] found that increasing the amount of $BaTiO_3$ in $BiFeO_3$ decreased the grain size, increased chemical homogeneity and hence increased the ferroelectric properties. As discussed above, all factors influencing the solid state sintering and the process of formation is not known, and further studies would be interesting. This information, together with explicitly identified solution limits and structural transformations, can lead to successful synthesis of pure-phase samples with high bismuth content. Also, there are alternative synthesis routes to be tried, such as solution routes, liquid-rapid sintering and the recently reported microwave-hydrothermal synthesis[63]. All properties should also be investigated as a function of level of substitution.

Last, it is important to mention that polycrystalline bulk material is not the only form that is interesting to study. Another form may be nanocrystals, but the most interesting form for application is probably thin films.

8 Acknowledgements

First of all, thanks to the whole “Oxide group”: my examiner Sten Eriksson, my supervisor Stefan Norberg, Francis Kinyanjui, Habibur Raman, Christopher Knee and our guest for nine months, Makoto Kobayashi. Thanks to Dongmei Zhao and Charlotte Bouveng at Environmental Inorganic Chemistry for answering all my questions. Special thanks to Stefan Norberg and Stephen Hull for help with the neutron TOF measurements and also to Roland Mathieu for performing the magnetization measurements.

9 References

1 Arunachalam, V. S. & Fleischer, E. L. Harnessing materials for energy - introduction. *Mrs Bull* **33**, 264-276 (2008).

2 Mitchell, R. H. *Perovskites - Modern and Ancient*. (Almaz Press Inc., 2002).

3 Schmid, H. Multi-ferroic magnetoelectrics. *Ferroelectrics* **164** (1994).

4 Zhao, T. *et al.* Electrical control of antiferromagnetic domains in multiferroic BiFeO3 films at room temperature. *Nature Materials* **5**, 823-829, doi:Doi 10.1038/Nmat1731 (2006).

5 Fiebig, M., Lottermoser, T., Frohlich, D., Goltsev, A. V. & Pisarev, R. V. Observation of coupled magnetic and electric domains. *Nature* **419**, 818-820, doi:Doi 10.1038/Nature01077 (2002).

6 Lottermoser, T. *et al.* Magnetic phase control by an electric field. *Nature* **430**, 541-544, doi:Doi 10.1038/Nature02728 (2004).

7 Nan, C. W., Liu, G., Lin, Y. H. & Chen, H. D. Magnetic-field-induced electric polarization in multiferroic nanostructures. *Phys Rev Lett* **94**, -, doi:Artn 197203
Doi 10.1103/Physrevlett.94.197203 (2005).

8 Kimura, T. *et al.* Magnetic control of ferroelectric polarization. *Nature* **426**, 55-58, doi:Doi 10.1038/Nature02018 (2003).

9 Eerenstein, W., Mathur, N. D. & Scott, J. F. Multiferroic and magnetoelectric materials. *Nature* **442**, 759-765 (2006).

10 Fiebig, M. Revival of the magnetoelectric effect. *J Phys D Appl Phys* **38**, R123-R152, doi:Doi 10.1088/0022-3727/38/8/R01 (2005).

11 Bibes, M. & Barthelemy, A. Multiferroics: Towards a magnetoelectric memory. *Nat Mater* **7**, 425-426 (2008).

12 Béa, H. & *et al*. Spintronics with multiferroics. *Journal of Physics: Condensed Matter* **20**, 434221 (2008).

13 Loidl, A. & *et al*. Multiferroics. *Journal of Physics: Condensed Matter* **20**, 430301 (2008).

14 Kleemann, W. & Borisov, P. in *Smart Materials for Energy, Communications and Security NATO Science for Peace and Security Series B: Physics and Biophysics* eds Igor A. Luk'yanchuk & Daoud Mezzane) 3-11 (Springer Netherlands, 2008).

15 Hill, N. A. Why are there so few magnetic ferroelectrics? *J Phys Chem B* **104**, 6694-6709, doi:Doi 10.1021/Jp000114x (2000).

16 Norberg, S. T., Hull, S., Mathieu, R. & Eriksson, S. G. Local structural properties of 0.5BiMnO(3)-0.5ATiO(3) (A = Ba or Sr). *Chem. Commun.* **46**, 1455-1457, doi:10.1039/b912519a (2010).

17 Woodward, P. M. Octahedral tilting in perovskites .1. Geometrical considerations. *Acta Crystallogr B* **53**, 32-43 (1997).

18 Goldschmidt, V. M. *Str. Nor. Vidensk. Akad. Oslo* **1** (1926).

19 Roth, R. S. Classification of Perovskite and Other Abo3-Type Compounds. *J Res Nat Bur Stand* **58**, 75-88 (1957).

20 Wood, E. A. Polymorphism in Potassium Niobate, Sodium Niobate, and Other Abo3 Compounds. *Acta Crystallogr* **4**, 353-362 (1951).

21 Jona, E. S., S. *Ferroelectric Crystals*. (Pergamon Press, 1962).

22 Smart, L. E., Moore, Elaine A. *Solid State Chemistry: An Introduction*. 3 edn, (Taylor and Francis, 2005).

23 Smolenskii, G. A., Isupov, V. A. & Agranovskaya, A. I. A NEW GROUP OF FERROELECTRICS - (WITH LAYERED STRUCTURE). *Soviet Physics-Solid State* **1**, 149-150 (1959).

24 Fiebig, M. & Spaldin, N. A. Current trends of the magnetoelectric effect. *Eur Phys J B* **71**, 293-297, doi:DOI 10.1140/epjb/e2009-00266-4 (2009).

25 Spaldin, N. A. & Fiebig, M. The renaissance of magnetoelectric multiferroics. *Science* **309**, 391-392, doi:DOI 10.1126/science.1113357 (2005).

26 Martin, L. *et al.* Multiferroics and magnetoelectrics: thin films and nanostructures. *J Phys-Condens Mat* **20**, -, doi:Artn 434220

Doi 10.1088/0953-8984/20/43/434220 (2008).
27 Ramesh, R. & Spaldin, N. A. Multiferroics: progress and prospects in thin films. *Nat Mater* **6**, 21-29 (2007).
28 Wang, K. F., Liu, J. M. & Ren, Z. F. Multiferroicity: the coupling between magnetic and polarization orders. *Adv Phys* **58**, 321-448, doi:Doi 10.1080/00018730902920554 (2009).
29 Filippetti, A. & Hill, N. A. Coexistence of magnetism and ferroelectricity in perovskites. *Phys Rev B* **65**, -, doi:Artn 195120
Doi 10.1103/Physrevb.65.195120 (2002).
30 Ederer, C. & Spaldin, N. A. Magnetoelectrics: A new route to magnetic ferroelectrics. *Nat Mater* **3**, 849-851 (2004).
31 Ramesh, R. Materials science: Emerging routes to multiferroics. *Nature* **461**, 1218-1219 (2009).
32 Cheong, S.-W. & Mostovoy, M. Multiferroics: a magnetic twist for ferroelectricity. *Nat Mater* **6**, 13-20 (2007).
33 Hill, N. A. & Filippetti, A. Why are there any magnetic ferroelectrics? *J Magn Magn Mater* **242**, 976-979, doi:Pii S0304-8853(01)01078-2 (2002).
34 Tabares-Munoz, C. R., J. -P.; Bezinges, A.; Monnier, A.; Schmid, H. Measurements of the qudratic Magnetoelectric effect on single crystalline BiFeO3. *Japanese Journal of Applied Physics* **24S2**, 1051-1053 (1985).
35 Kumar, M. M., Palkar, V. R., Srinivas, K. & Suryanarayana, S. V. Ferroelectricity in a pure BiFeO3 ceramic. *Applied Physics Letters* **76**, 2764-2766 (2000).
36 Neaton, J. B., Ederer, C., Waghmare, U. V., Spaldin, N. A. & Rabe, K. M. First-principles study of spontaneous polarization in multiferroic BiFeO3. *Phys Rev B* **71**, -, doi:Artn 014113
Doi 10.1103/Physrevb.71.014113 (2005).
37 Sosnowska, I., Peterlinneumaier, T. & Steichele, E. Spiral Magnetic-Ordering in Bismuth Ferrite. *J Phys C Solid State* **15**, 4835-4846 (1982).
38 Hill, N. A., Battig, P. & Daul, C. First principles search for multiferroism in BiCrO3. *J Phys Chem B* **106**, 3383-3388, doi:Doi 10.1021/Jp013170m (2002).
39 Belik, A. A. *et al.* Neutron powder diffraction study on the crystal and magnetic structures of BiCrO3. *Chem Mater* **20**, 3765-3769, doi:Doi 10.1021/Cm800375d (2008).
40 Cohen, R. E. & Krakauer, H. ELECTRONIC-STRUCTURE STUDIES OF THE DIFFERENCES IN FERROELECTRIC BEHAVIOR OF BATIO3 AND PBTIO3. *Ferroelectrics* **136**, 65-83 (1992).
41 Megaw, H. D. Origin of Ferroelectricity in Barium Titanate and Other Perovskite-Type Crystals. *Acta Crystallogr* **5**, 739-749 (1952).
42 Koonce, C. S., Cohen, M. L., Schooley, J. F., Hosler, W. R. & Pfeiffer, E. R. Superconducting Transition Temperatures of Semiconducting SrTiO_{3}. *Physical Review* **163**, 380 (1967).
43 Shevchuk, Y. A., Gagulin, V. V., Korchagina, S. K. & Ivanova, V. V. SrTiO3-BiCrO3 solid solutions: Synthesis, X-ray diffraction study, and dielectric properties in the microwave range. *Inorg. Mater.* **36**, 739-741 (2000).
44 Smith, R. T., Achenbac.Gd, Gerson, R. & James, W. J. Dielectric Properties of Solid Solutions of Bifeo3 with Pb(Ti,Zr)O3 at High Temperature. *J Appl Phys* **39**, 70-& (1968).
45 Kumar, M. M., Srinivas, A. & Suryanarayana, S. V. Structure property relations in BiFeO3/BaTiO3 solid solutions. *J Appl Phys* **87**, 855-862 (2000).
46 Ianculescu, A. *et al.* Preparation and magnetic properties of the (1-x)BiFeO3-xBaTiO(3) solid solutions. *J. Optoelectron. Adv. Mater.* **10**, 1805-1809 (2008).
47 Kumar, M. M., Srinivas, A., Suryanarayana, S. V. & Bhimasankaram, T. Dielectric and impedance studies on BiFeO3-BaTiO3 solid solutions. *Phys Status Solidi A* **165**, 317-326 (1998).
48 Fujii, T., Jinzenji, S., Asahara, Y., Kajima, A. & Shinjo, T. Magnetic-Properties of Bifeo3-Batio3 and Bifeo3-Pbti(Zr)O3 Glassy Sputtered Films. *J Appl Phys* **64**, 5434-5436 (1988).
49 Fedulov, S. A., Ladyzhinskii, P. B., Pyatigorskaya, I. L. & Venevtsev, Y. N. Complete Phase Diagram of the Pbtio3-Bifeo3 System. *Soviet Physics-Solid State* **6**, 375-378 (1964).

50 Ivanov, S. A., Nordblad, P., Tellgren, R. & Ritter, C. Magnetoelectric perovskite (Bi0.5Pb0.5)(Fe0.5Zr0.5)O3: Preparation, structural and magnetic properties. *Solid State Sciences* **12**, 115-122, doi:DOI: 10.1016/j.solidstatesciences.2009.10.015 (2010).
51 Woolfson, M. M. *An Introduction to X-ray Crystallography*. 2 edn, (Cambridge University Press, 1997).
52 Copley, R. D. *The Fundamentals of Neutron Powder Diffraction*. (National Institute of Standards an Technology, 2001).
53 Kittel, C. *Introduction to Solid State Physics*. 7 edn, (John Wiley & Sons, Inc., 1996).
54 Bacon, G. E. *Neutron diffraction*. 3 edn, (Oxford university Press, 1975).
55 Lovesey, S. W. *Theory of neutron scattering from condensed matter*. Vol. 1 (Clarendon Press, 1984).
56 Rietveld, H. M. A Profile Refinement Method for Nuclear and Magnetic Structures. *J Appl Crystallogr* **2**, 65-& (1969).
57 Young, R. A. *The Rietveld Method*. (Oxford university Press, 1993).
58 General Structure Analysis System (GSAS) (Los Alamos National Laboratory Report LAUR 86-748, 2004).
59 Hull, S. *et al.* The Polaris Powder Diffractometer at Isis. *Physica B* **180**, 1000-1002 (1992).
60 Buscaglia, M. T. *et al.* Preparation and characterisation of the magneto-electric xBiFeO(3)-(1-x)BaTiO3 ceramics. *Journal of the European Ceramic Society* **26**, 3027-3030, doi:10.1016/j.jeurceramsoc.2006.02.023 (2006).
61 Yoneda, Y., Yoshii, K., Kohara, S., Kitagawa, S. & Mori, S. Local structure of BiFeO3-BaTiO3 mixture. *Japanese Journal of Applied Physics* **47**, 7590-7594, doi:Doi 10.1143/Jjap.47.7590 (2008).
62 Schmidt, R., Eerenstein, W., Winiecki, T., Morrison, F. D. & Midgley, P. A. Impedance spectroscopy of epitaxial multiferroic thin films. *Phys Rev B* **75**, 245111 (2007).
63 Prado-Gonjal, J., Villafuerte-Castrejon, M. E., Fuentes, L. & Moran, E. Microwave-hydrothermal synthesis of the multiferroic BiFeO3. *Mater Res Bull* **44**, 1734-1737, doi:DOI 10.1016/j.materresbull.2009.03.015 (2009).